國立臺灣大學電機資訊學院光電工程學研究所

碩士論文

Graduate Institute of Photonics and Optoelectronics

College of Electrical Engineering and Computer Science

National Taiwan University

Master's Thesis

氫氧化四甲基銨側壁處理之微米級氮化銦鎵/氮化鋁鎵紫外光發光二極體研究

Investigation of micron-sized InGaN/AlGaN ultraviolet light emitting diode with tetramethylazanium hydroxide sidewall treatment

張皓任

Chang, Hao-Jen

指導教授：林建中 博士

Advisor: Lin, Chien-Chung Ph.D.

中華民國一百一十三年十二月

December 2024

doi:10.6342/NTU202500064

致謝

我想要向在台大光電所的這兩年多一路上幫助我、支持我的人道謝，首先最感謝的是實驗室指導教授林建中教授，在這段時間裡，從碩一的發光半導體物理、雷射原理到碩二做實驗的過程，再到最後修改論文的來來回回，我學到了大量的知識與做人處事的道理。除了每周的 meeting 以外，我也時常跑去辦公室找老師討論實驗內容，老師總是很有耐心地給我意見，並包容我偶爾的疏失。

第二個要感謝新穎光電實驗室的同學，雖然我們一路上遇到了不少困難，經費短缺、儀器壞掉等等，但我們最終都一一克服，一起走到這，回想起大家一起在無塵室做製程，一起互相加油打氣還蠻快樂的，謝謝你們讓我研究所的這兩年多不孤單。再來要感謝學長們，手把手的帶著我做製程，即便是趕畢業的時候也沒有棄我於不顧，甚至畢業後也很願意在實驗上給我建議及幫助。最後也謝謝 micro-LED 組的兩位學弟，常常幫我們做很繁瑣的量測，祝福你們能夠準時畢業。

doi:10.6342/NTU202500064

摘要

使用在光鋐科技股份有限公司購買之紫外光波長的InGaN/AlGaN磊晶片製造方形發光區域的微米等級發光二極體，本實驗製程的元件有多個尺寸，發光區域的邊長有3μm、5μm、10μm、15μm、20μm、25μm、50μm、75μm以及100μm。整套實驗包含了元件及光罩設計、製程，還有最後的電性和光學量測。

在p型電極及p型半導體之間加入一層氧化銦錫透明導電層來增加電流流經元件的均勻性，同時可以縮小p型電極在發光區域上覆蓋的面積，以減少被電極遮住的光子。在乾蝕刻元件以後，我們將晶片泡入氫氧化四甲基銨(TMAH)中濕蝕刻，可以消除感應耦合式電漿蝕刻(ICP-RIE)對元件造成的側壁缺陷，將側壁平坦化，如此一來便能減少側壁的表面非輻射複合，達到外部量子效率的提升，另外，消除缺陷的同時也可以一併使得元件的漏電流縮小。

關鍵詞:紫外光發光二極體、氧化銦錫、側壁缺陷、外部量子效率、漏電流

doi:10.6342/NTU202500064

Abstract

In this experiment, micro-scale light-emitting diodes (LEDs) with square light-emitting areas were manufactured using InGaN/AlGaN epitaxial wafers, with ultraviolet wavelengths. The devices in this experimental process come in various sizes, with the side lengths of the light-emitting areas being 3μm, 5μm, 10μm, 15μm, 20μm, 25μm, 50μm, 75μm, and 100μm. The entire experiment includes device and mask design, processing, and final electrical and optical measurements.

To increase the uniformity of current flowing through the device, indium tin oxide (ITO) transparent conductive layer was added between the p-type electrode and the p-type semiconductor. This also allows for a reduction in the area covered by the p-type electrode over the light-emitting region, minimizing the blockage of photons. After dry etching the device, the wafer was immersed in tetramethylammonium hydroxide (TMAH) for wet etching, which eliminates sidewall defects caused by inductively coupled plasma etching (ICP-RIE) and flattens the sidewalls. This reduces surface non-radiative recombination on the sidewalls, leading to an improvement in external quantum efficiency. Additionally, while eliminating defects, it also helps to reduce the leakage current of the device.

doi:10.6342/NTU202500064

Keywords: Ultraviolet light-emitting diodes, indium tin oxide, sidewall defects, external quantum efficiency, leakage current, tetramethylammonium hydroxide.

doi:10.6342/NTU202500064

Content

doi:10.6342/NTU202500064

doi:10.6342/NTU202500064

doi:10.6342/NTU202500064

List of Figure

doi:10.6342/NTU202500064

doi:10.6342/NTU202500064

doi:10.6342/NTU202500064

doi:10.6342/NTU202500064

doi:10.6342/NTU202500064

doi:10.6342/NTU202500064

List of Tables

doi:10.6342/NTU202500064

Chapter 1 Introduction

1.1 Introduction and evolution of Light emitting diode (LED)

A light-emitting diode (LED) is a semiconductor device that emits light. In 1907, Henry Joseph Round discovered that silicon carbide (SiC), originally used as an abrasive, emitted light when an electric current passed through it. This marked the beginning of LED technology, although the mechanism of light emission was not well understood at the time. Subsequently, scientists began to study the light-emitting properties of SiC and II-VI compound semiconductors. In the 1920s, a 20-year-old Russian experimentalist, Oleg Vladimirovich Lossev, published a paper on electroluminescence. His report was the first detailed study of semiconductor electroluminescence.[1] In 1995, the first III-V compound semiconductor was invented by Braustein A significant breakthrough occurred in 1962 when GE, Monsanto, and IBM's research labs collaborated to develop red-emitting gallium arsenide phosphide (GaAsP) semiconductor compounds, marking the beginning of commercial LEDs. In the mid-1990s, Shuji Nakamura made the first blue and green double heterostructure LEDs by employing III-V nitride materials and metalorganic chemical vapor deposition methods to grow gallium nitride (GaN) and

doi:10.6342/NTU202500064

indium gallium nitride (InGaN) on sapphire substrates.[2] These types of LEDs were widely adopted thereafter. Following the invention of short-wavelength LEDs, scientists began developing white light LEDs using three methods: combining red, green, and blue LEDs to produce white light, using UV light to excite phosphors that emit the three primary colors, and using blue light to illuminate yellow phosphors.[3] Over time, LEDs have progressed from producing only red light to offering a broad spectrum of emissions, including visible light, infrared, ultraviolet, and beyond. Additionally, their brightness and efficiency have significantly improved.

With the development of LEDs, there are more and more applications of LED technology in our daily lives. Initially, LED lights were used to replace traditional lighting and indicator light sources with energy-efficient options that have a longer lifetimes.[4] Subsequently, replace the display light source from LCD (Liquid Crystal Display) or OLED (Organic LED) with brighter LED that has a wider color gamut. As people pursue higher resolution displays, micro-size LEDs have become essential to meet these demands.[5] To accommodate the upcoming developments in head-wearing displays such as AR (Augmented Reality), VR (Virtual Reality), and MR (Mixed Reality), micro-LED technology will undoubtedly play a crucial role.

doi:10.6342/NTU202500064

Advances in semiconductor process technology have allowed us to produce smaller and smaller micro-LEDs, ensuring that displays have a high enough Pixel Per Inch (PPI).

1.2 Motivation

UV micro-LEDs can be classified based on their emission wavelength into deep UV (DUV, 200–300 nm) and near UV (NUV, 300–400 nm), or further subdivided into UVA (320-400 nm), UVB (280-320 nm), and UVC (200-280 nm). In recent years, the COVID-19 virus has brought significant attention to deep ultraviolet light-emitting diodes (UV LEDs) that can help with disinfection, leading to increased interest in the development of UV LEDs.[6] Additionally, micro-sized UV LEDs have many extra applications, such as optical communication, time-resolved fluorescence detection, and maskless direct writing.[7] Furthermore, using UV micro-LEDs to excite quantum dots can lead to higher resolution for the next generation of displays.[8]

To meet the diverse demands for UV micro-LEDs, we designed devices of various sizes. After mesa dry etching, we used tetramethylammonium hydroxide (TMAH) wet etching to reduce sidewall defects. We also measured the impact of this fabrication method on the electrical properties and efficiency of the devices.

doi:10.6342/NTU202500064

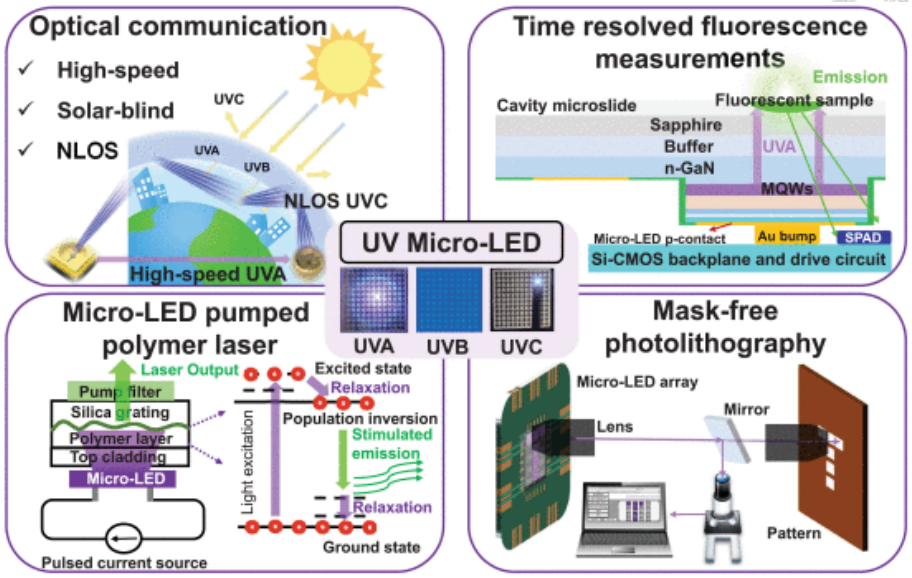

Figure 1 Several specific applications of UV micro-LEDs.[7]

TMAH can smooth the mesa sidewalls after etching, as described in the study by Y. Li et al.[9] In their research, the RMS roughness of their AlGaN material after etching was 0.230 nm, but after TMAH wet etching, it decreased to 0.173 nm. Another paper also mentions that, in addition to surface flattening, TMAH wet etching can also remove native oxide and nitrogen vacancy-related dangling bonds from the GaN surface.[10] Therefore, we expect that TMAH sidewall treatment can enhance the overall performance of the device.

doi:10.6342/NTU202500064

1.3 Operational principles of a light-emitting-diode (LED)

We first dope semiconductor materials with different components to form P-type and N-type semiconductors, which are then connected together to create a PN junction (diode). When the diode is forward biased, holes from the P-type material and electrons from the N-type material are driven into the active region between the two semiconductor layers. In this area, they combine and release energy in the form of photons. This light emission occurs through a solid-state process known as electroluminescence.[11]

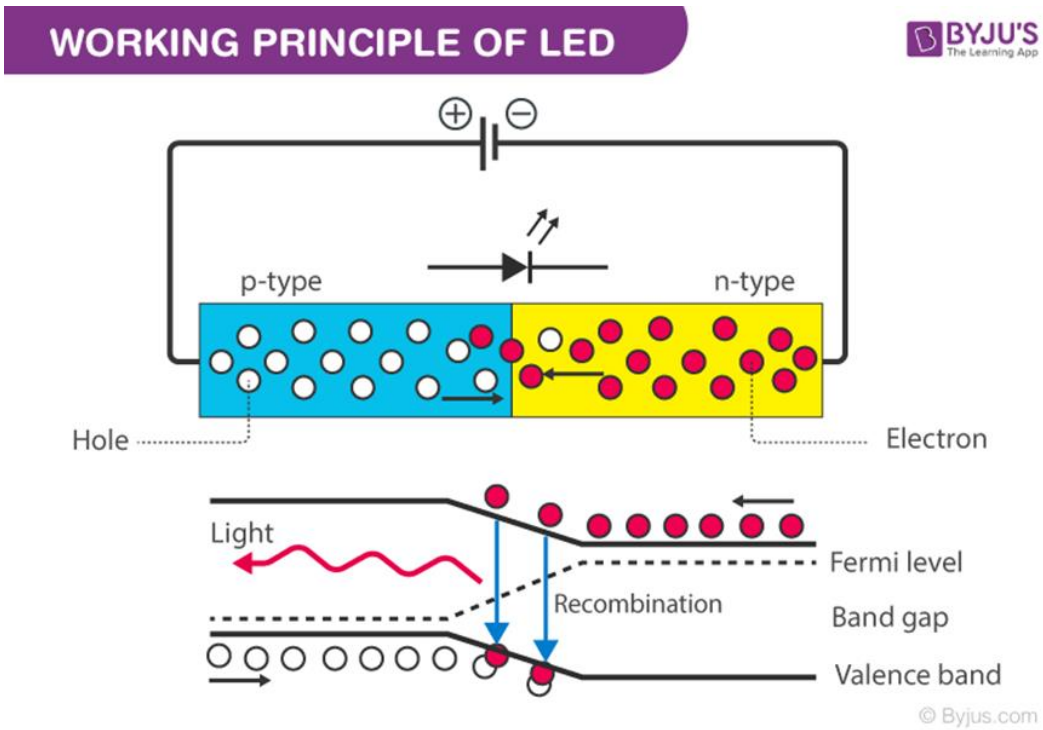

Figure 2 LED operating principle.[12]

doi:10.6342/NTU202500064

The recombination of holes and electrons at the p-n junction occurs when electrons transition from the conduction band to the valence band. A larger energy difference between these bands results in the emission of higher-energy light, which corresponds to shorter wavelengths. Because this energy difference, known as the band gap, varies with the semiconductor material, the selection of LED materials is based on their band gap to achieve the desired color of light. For example, Gallium nitride can emit blue light due to its band gap of 3.4 eV, while aluminum gallium arsenide is capable of producing red light because its band gap is 1.4 eV.

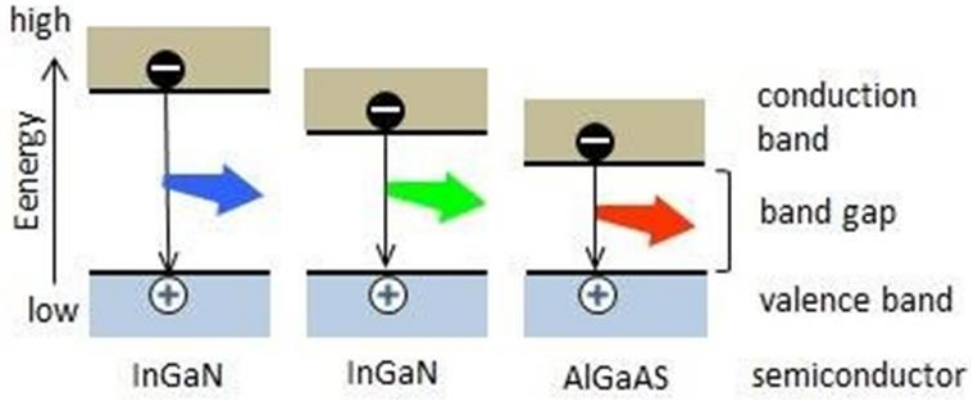

Figure 3 Comparison of band gap energies possessed by common blue, green, and red LED materials.[13]

A diode is considered forward-biased when the voltage across it, i.e., $V_D>0$. In this state, the current flowing through the diode, I_D, is related to the voltage by the Shockley

doi:10.6342/NTU202500064

equation, which describes the behavior of the diode until it reaches the breakdown region. In reverse bias, the diode allows very little current to flow. However, when the reverse voltage exceeds a certain level, known as the breakdown voltage, the diode experiences a rapid increase in current.

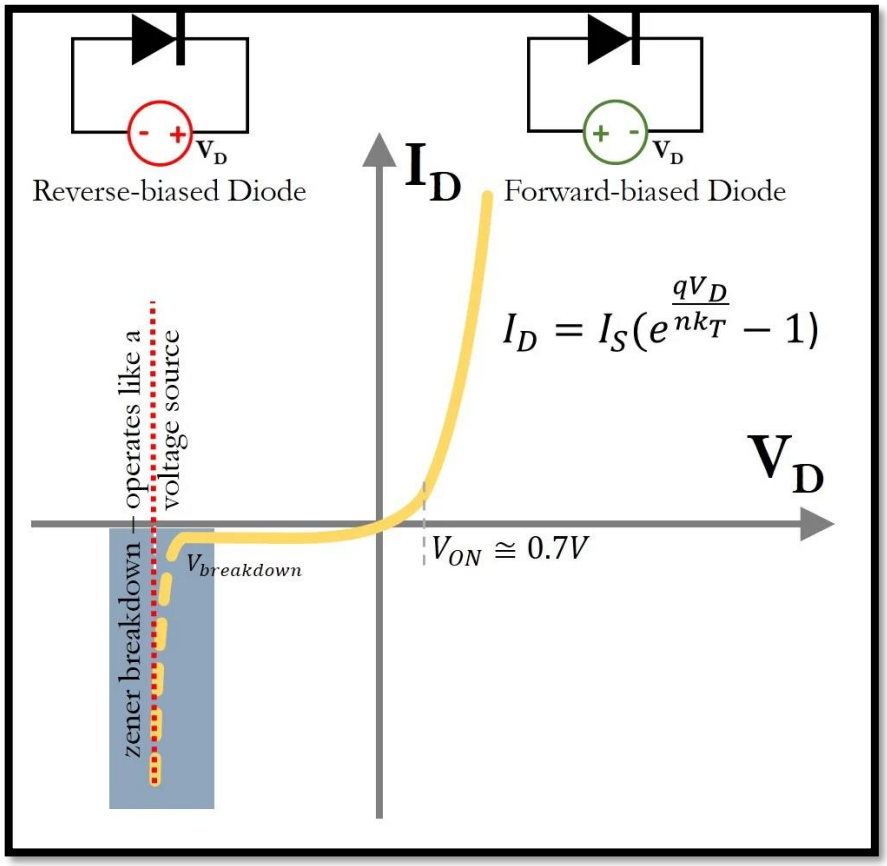

Figure 4 current versus voltage curve for a diode.[14]

doi:10.6342/NTU202500064

1.4 Reference Review

The first article is written by David Huang et al.[15] This experiment fabricated micro-LEDs in six sizes ranging from 10 μm to 100 μm and studied the impact of mesa size on various aspects of EQE. The experiment found that due to the higher perimeter-to-area ratio of smaller devices, the influence of sidewall defects is more pronounced for them. The EQE of smaller devices is lower than that of larger ones, and a higher current density is required to reach the EQE peak. However, the smaller devices have more uniform current spreading, so the efficiency droop is not as significant as that of larger devices.

doi:10.6342/NTU202500064

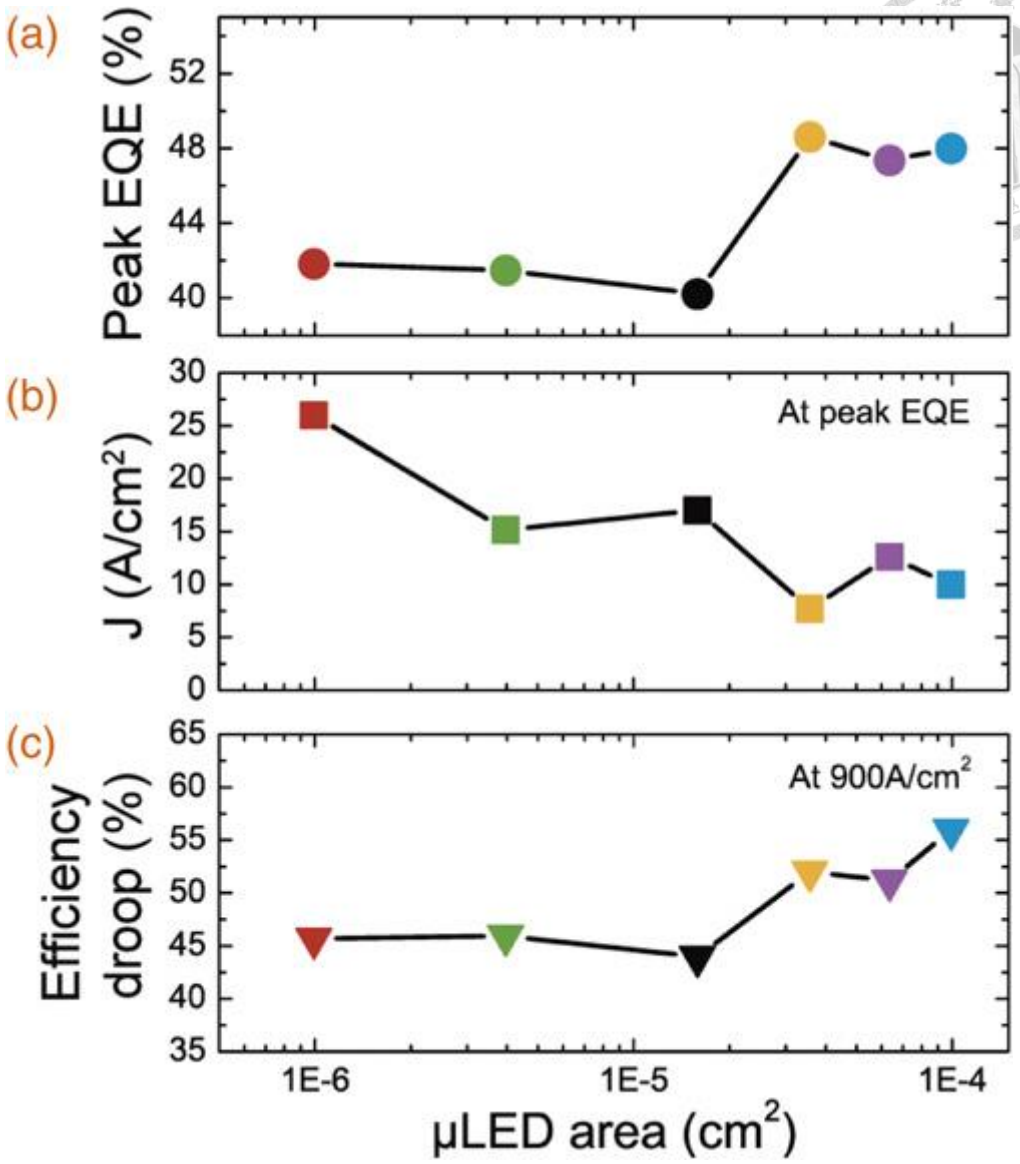

Figure 5 (a) Peak EQE, (b) current density at the peak EQE, and (c) efficiency droop at 900 A/cm² of the μLEDs.[15]

The next study is by Matthew S. Wong et al.[16], who discussed the impact of sidewall treatment on devices. For devices with sidewall treatments, an Al2O3 passivation layer deposited by ALD was employed for surface treatment. Additionally, another treatment

doi:10.6342/NTU202500064

utilized a TMA/nitrogen plasma process. For the 100 μm devices, there was not much difference observed under reverse bias. However, devices with sidewall treatments demonstrated superior forward current-voltage characteristics compared to those without such treatments. At a current density of 20 A/cm², the voltage readings were 3.0 V for the 100×100 μm² devices without sidewall passivation, 2.6 V for those with ALD sidewall passivation, and 2.3 V for devices treated with both TMA/nitrogen plasma and ALD sidewall passivation. For the 20 μm devices, the benefits of ALD became more significant, effectively suppressing reverse leakage current, while the TMA/nitrogen plasma treatment also improved the performance of the devices under forward bias.

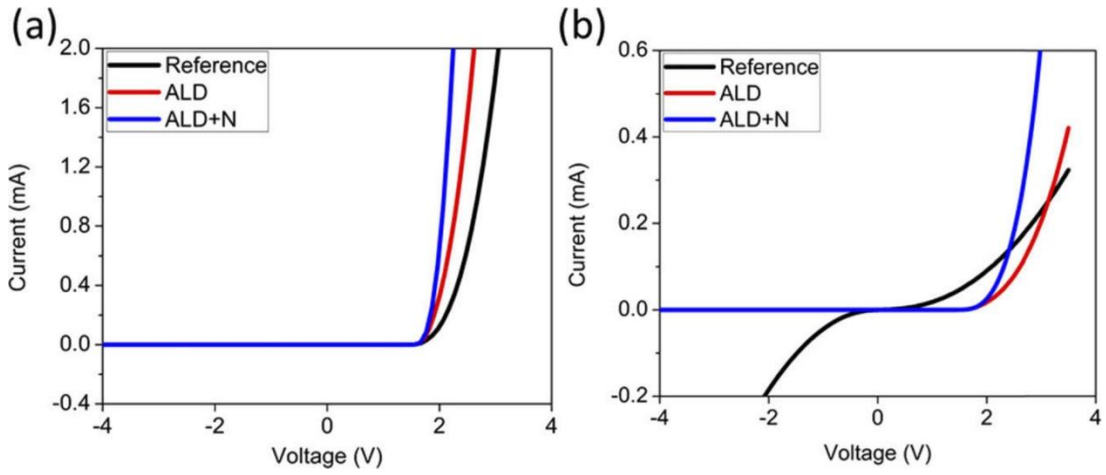

Figure 6 IV characteristics of (a) 100 and (b) 20 μm micro-LEDs with different sidewall treatment.[16]

doi:10.6342/NTU202500064

The next research is written by J. Kuo et al.[17] They compared the effects of sidewall damage on devices of different sizes. First, for devices dimension of 100μm x 100μm, 60μm x 60μm, and 20μm x 20μm, a 4μm wide damage region was added, resulting in usable areas of 85%, 75%, and 36% of the original size, respectively. In this situation, the greatest impact was observed in hole concentration. As shown in the graph, without sidewall damage, the hole concentration in the MQW region increases as the devices size decreases due to current spreading. However, when considering sidewall damage, the hole concentration of smaller devices declines rapidly. This phenomenon leads to a subsequent decrease in EQE and an increase in leakage current.

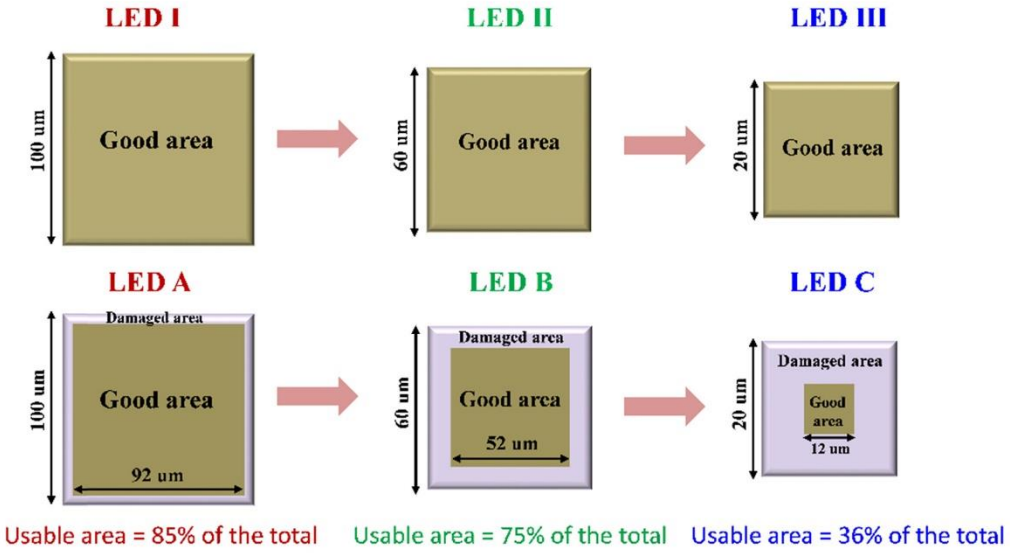

Figure 7 schematic diagram for LED I, II, II w/o sidewall damages and A, B, C w/ sidewall damages.[17]

doi:10.6342/NTU202500064

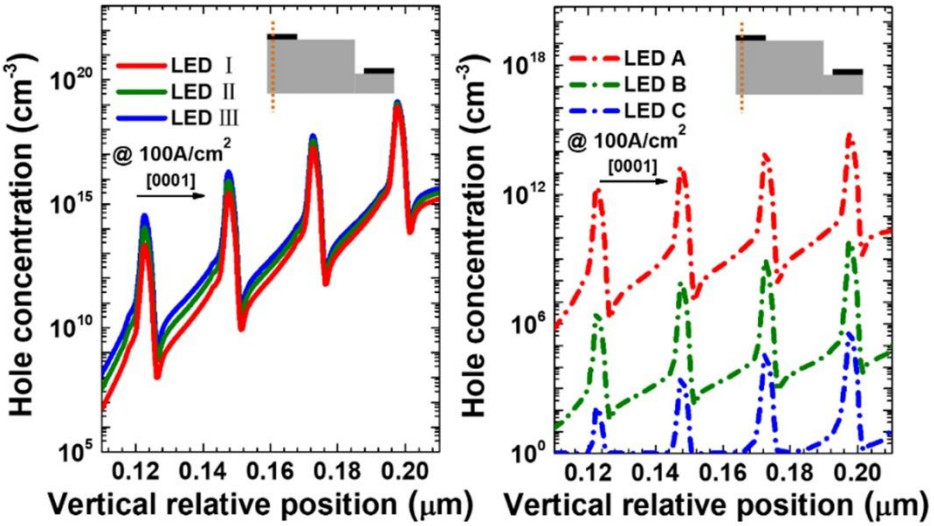

Figure 8 calculated hole concentration for LEDs. The current density is 100A/cm^2.[17]

Next research is published by Tzu-Yi Lee et al.[18]. They fabricated InGaN-based blue LEDs in various sizes ranging from 5 × 5 μm² to 100 × 100 μm² to investigate how atomic layer deposition (ALD) improves the devices. Among the ABC model parameters, the Shockley-Read-Hall (SRH) recombination coefficient A is important due to surface recombination, and it is also size-dependent. According to the experimental data, they created a graph showing the relationship between the SRH coefficient and mesa size, which indicates that smaller devices have a larger SRH coefficient. Additionally, ALD devices have a lower A value. By calculating the slope, they found that the surface

doi:10.6342/NTU202500064

recombination velocities for ALD and non-ALD devices are 551.3 cm/s and 1026 cm/s, respectively.

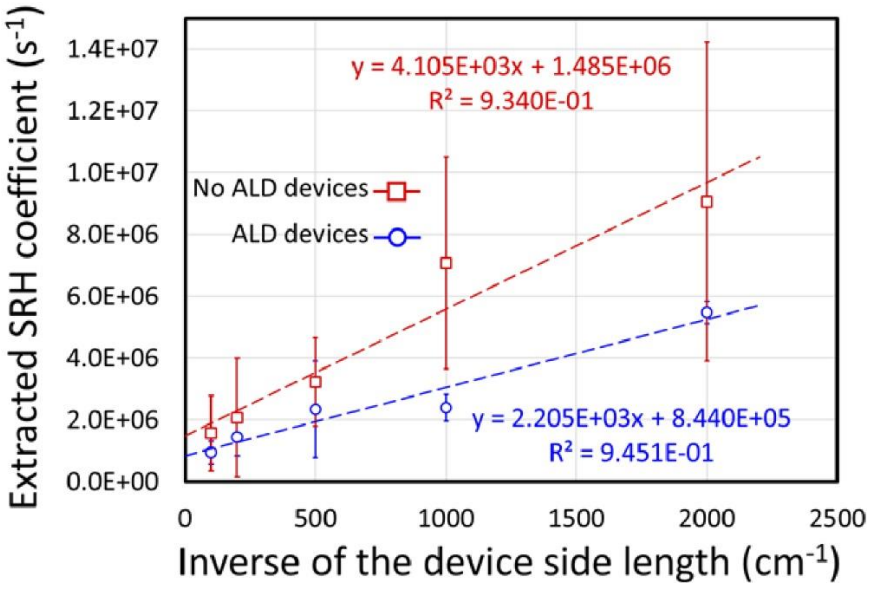

Figure 9 the SRH coefficient w/ and w/o ALD.[18]

doi:10.6342/NTU202500064

Chapter 2 Experiment principles and instruments

2.1 Schottky contact and ohmic contact

When metal and semiconductor come into contact, a barrier is formed that prevents the flow of electrons. This energy barrier at the contact interface is called the Schottky barrier Φ_{B0}, which is determined by the work function of the metal Φ_m and the electron affinity of the semiconductor material χ. It can be expressed by the following equation:

$$\Phi_{B0} = \Phi_m - \chi [19]$$

Taking n-type semiconductor as an example, when the work function of the metal $\Phi_m >$ the work function of the semiconductor Φ_s, the contact interface is a Schottky contact. Conversely, if the work function of the metal is less than that of the semiconductor, it is considered an ohmic contact.

Choosing the correct metal material to correspond with the semiconductor material can effectively eliminate the energy barrier at the contact interface, forming an ohmic contact. This allows the flow of electrons to follow a linear relationship according to Ohm's law, reducing the energy loss caused by the Schottky barrier and lowering contact resistance,

doi:10.6342/NTU202500064

thereby enhancing the performance of the device. Therefore, selecting the appropriate metal for the semiconductor during the manufacturing process is extremely important.

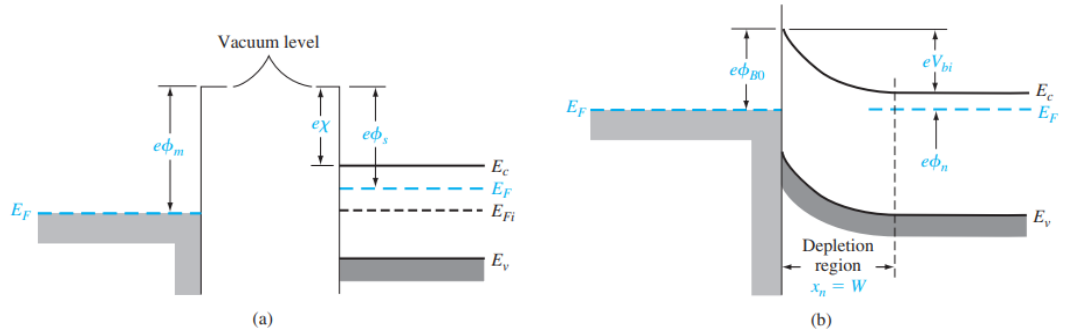

Figure 10 (a) Energy-band diagram before contact; (b) energy-band diagram of a metal n-type semiconductor junction for $\Phi_m > \Phi_s$.[20]

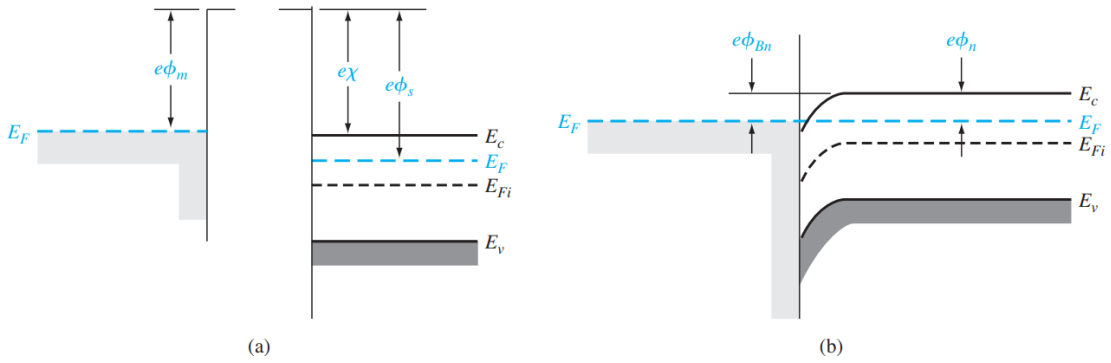

Figure 11 (a) Energy-band diagram before contact, (b) energy-band diagram of a metal n-type semiconductor junction for $\Phi_m > \Phi_s$.[20]

doi:10.6342/NTU202500064

2.2 current crowding effect

GaN/InGaN light-emitting diodes are typically grown on insulating sapphire or conductive SiC substrates. The SiC substrate offers advantages such as high conductivity and better lattice match to GaN. However, since SiC absorbs the light emitted by the LEDs and is more expensive, most current LEDs are still grown on sapphire substrates.[21].

Because the substrate is non-conductive, the p-electrode and n-electrode must be designed to be side by side. This design causes the pn junction current to be non-uniform and to crowd near the edges of the metal. This phenomenon is called the current crowding effect, which leads to an uneven current distribution, resulting in lower light intensity in areas farther away from the contacts.

doi:10.6342/NTU202500064

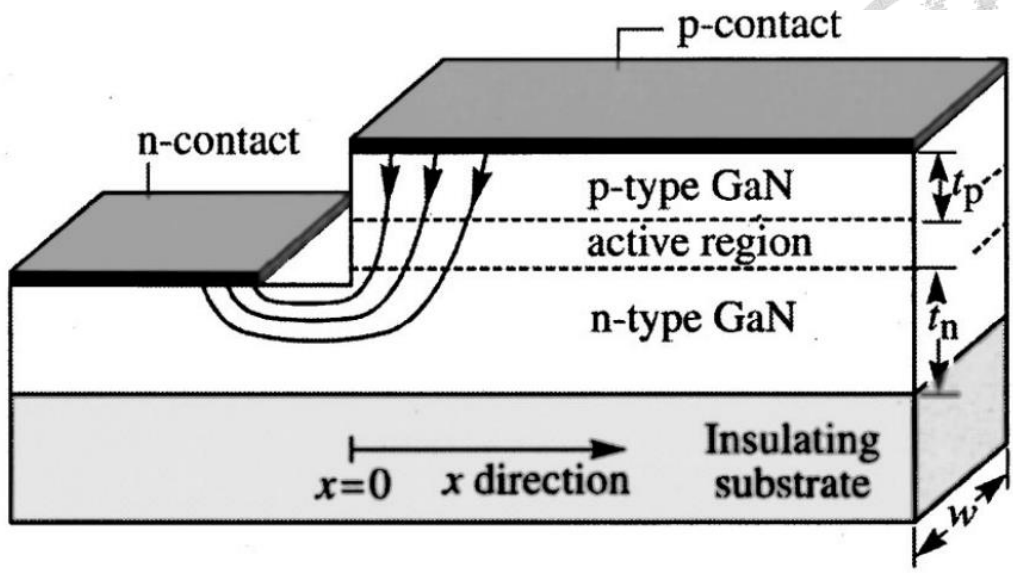

Figure 12 Illustration of GaN/InGaN LED structure with lateral current spreading.[22]

To address this issue, we grew a layer of Indium Tin Oxide (ITO) on the p-type GaN as a current spreading layer. When the current flows through this layer, it spreads uniformly down to the active region. Additionally, we designed an n-electrode that surrounds the mesa, which also helps to ensure that the current flows evenly.

2.3 Photolithography

Photolithography is a technique widely used in semiconductor manufacturing. This process can precisely transfer tiny patterns onto a wafer through exposure. A photomask is typically used as a mask to divide the wafer into exposed and non-exposed areas. When light is applied, the photosensitive photoresist on the wafer undergoes a chemical change.

doi:10.6342/NTU202500064

Subsequently, parts of the photoresist are dissolved in a developer solution, allowing the definition of small geometric patterns.

Photoresist is a photosensitive material that contains a solvent, sensitizer, and polymer. It can be divided into two types: positive photoresist and negative photoresist. In positive photoresist, the areas exposed to light become more soluble in the developer, while the unexposed areas remain. Conversely, in negative photoresist, the exposed areas dissolve, leaving the unexposed regions intact. The advantage of positive photoresist is its higher precision, making it suitable for creating smaller patterns, while negative photoresist offers benefits such as lower cost and shorter processing times

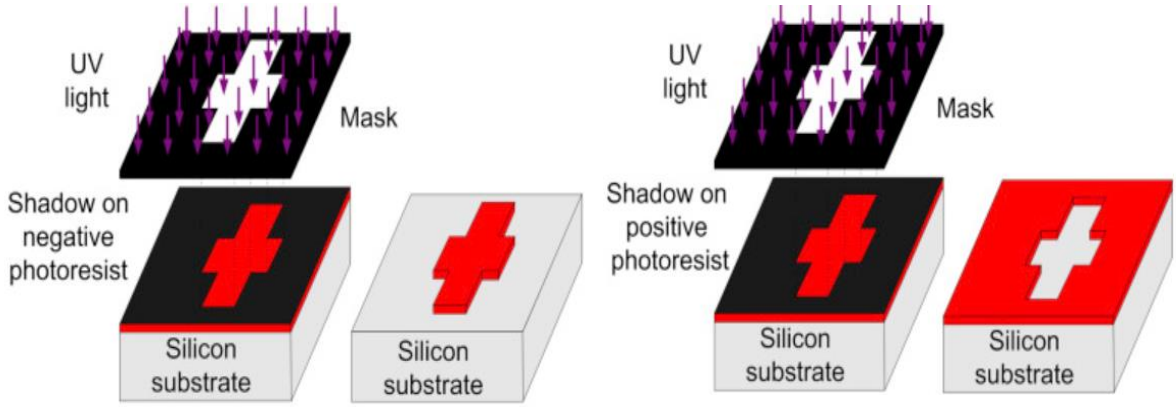

Figure 13 diagram of negative and positive photoresist.[23]

The thickness of the photoresist is influenced by the rotation speed and spinning duration of the spin coater. Additionally, different types of photoresists exhibit various degrees of stickiness and properties, making them suitable for different applications.

doi:10.6342/NTU202500064

Here are the steps of photolithography:

1. Wafer cleaning: remove contaminants or particles that may affect subsequent
2. HMDS & photoreist coating: A layer of Hexamethyldisilazane (HMDS) is applied in advance to enhance the adhesion of the photoresist.
3. Photoresist coating: Using a spin coater, the photoresist is uniformly applied to the wafer.
4. Soft bake: The first bake which done just after spin coating is called soft bake. It can make the photoresist more solid.
5. Alignment: Align the wafer with the pattern on the photomask.
6. Exposure: The photoresist in the areas not blocked by the photomask is exposed to light and undergoes a chemical change.
7. Development: Place the wafer in a developer solution to selectively dissolve either the exposed or unexposed areas of the photoresist, depending on whether a positive or negative resist is used.
8. Hard bake: Reduce the solvent content in the photoresist to enhance adhesion and minimize defects.

doi:10.6342/NTU202500064

2.4 Etching

Etching is a process used to remove specific areas of a wafer, allowing for the creation of structures or patterns on the material's surface. It is typically divided into dry etching and wet etching.

Dry etching utilizes gas molecules along with ions or free radicals generated to physically bombard or chemically react with the material on the wafer, allowing for the removal of the desired etched portions. This process can achieve vertical etching of the wafer surface, resulting in anisotropic etching.

Wet etching involves immersing the wafer in a chemical solution, which corrodes the material that needs to be removed. This isotropic etching cannot control the direction of etching, making it prone to significant lateral etching effects.

The advantage of dry etching is its ability to achieve anisotropic etching, allowing for more precise patterning, making it widely used in processes involving small feature sizes. However, a drawback is that it can result in a rougher etched surface.

doi:10.6342/NTU202500064

Wet etching offers better etching selectivity, faster etching rates, and lower costs. However, its isotropic etching nature limits its ability to create patterns with very small feature sizes.

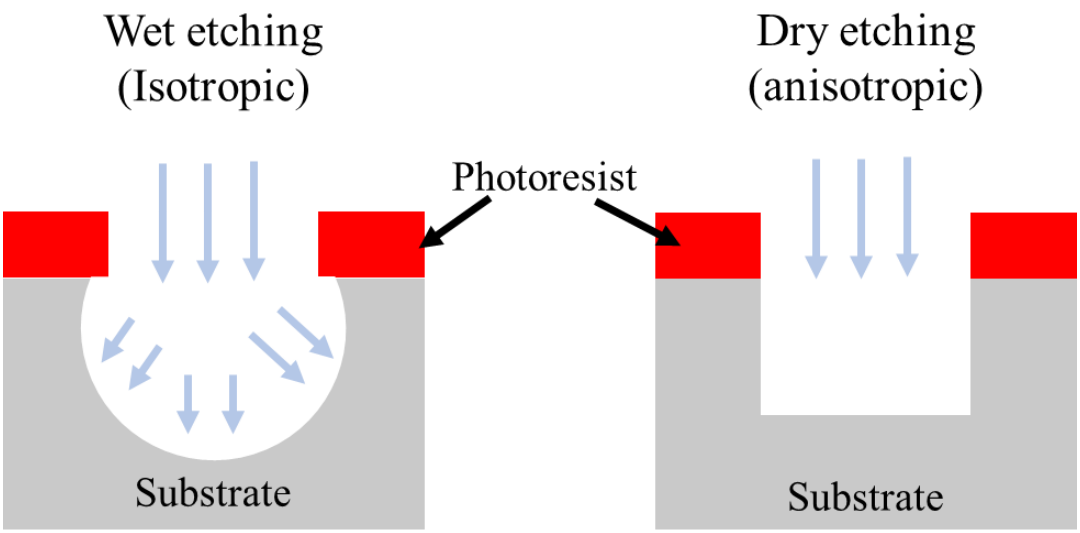

Figure 14 The schematic of the isotropic wet etching (left) and anisotropic dry etching (right).[24]

2.5 Plasma Enhanced Chemical Vapor Deposition (PECVD)

PECVD (Plasma-Enhanced Chemical Vapor Deposition) is a type of CVD (Chemical Vapor Deposition) technique. It typically involves applying a radio frequency voltage between two electrode plates, which generates electrons that collide with gas molecules in the chamber, forming a high-energy plasma state. This plasma contains reactive species

doi:10.6342/NTU202500064

such as free radicals and positive ions. These highly reactive products then deposit onto the substrate surface to form a thin film, while the vacuum pump removes any remaining by-products.

The properties of the thin film, such as type and thickness, can be precisely controlled by adjusting gas flow rates, radio frequency power, deposition temperature, and time. Compared to traditional CVD, PECVD allows for processing at lower temperatures due to the assistance of plasma, making it suitable for substrates that cannot withstand high temperatures.

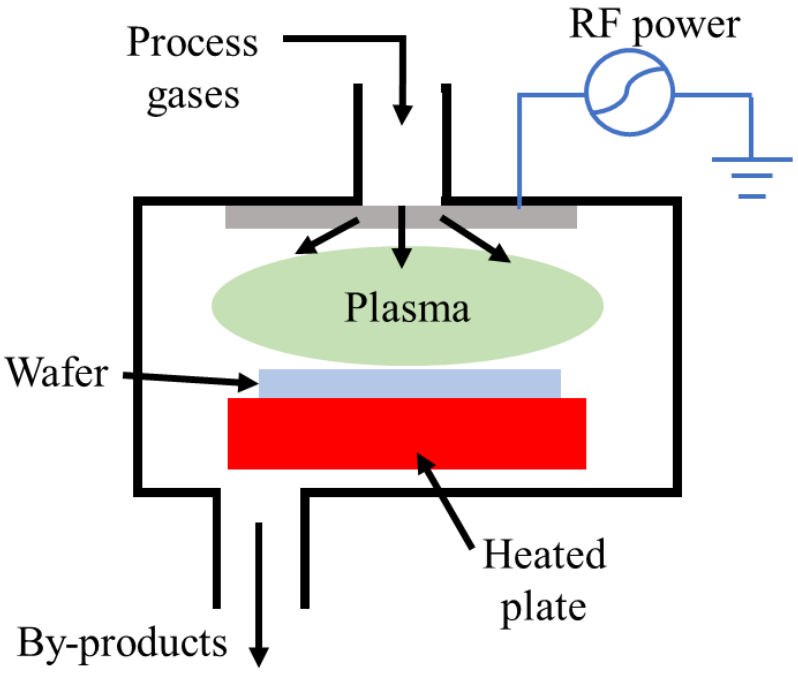

Figure 15 Schematic view of a typical PECVD reactor.[25]

doi:10.6342/NTU202500064

2.6 Electron Beam Evaporation

Electron beam evaporation, also known as E-beam, is a type of physical vapor deposition (PVD). It uses high-voltage electricity to generate electrons from a tungsten filament, which are then redirected by a magnetic field to strike a metal in a crucible. The kinetic energy of the high-energy electron beam is converted into thermal energy, melting the material. Once the target material transitions from a solid to a gaseous state, it deposits onto a substrate. By adjusting the acceleration voltage and monitoring with a quartz crystal oscillator, the thickness of the film and the deposition rate can be accurately controlled.

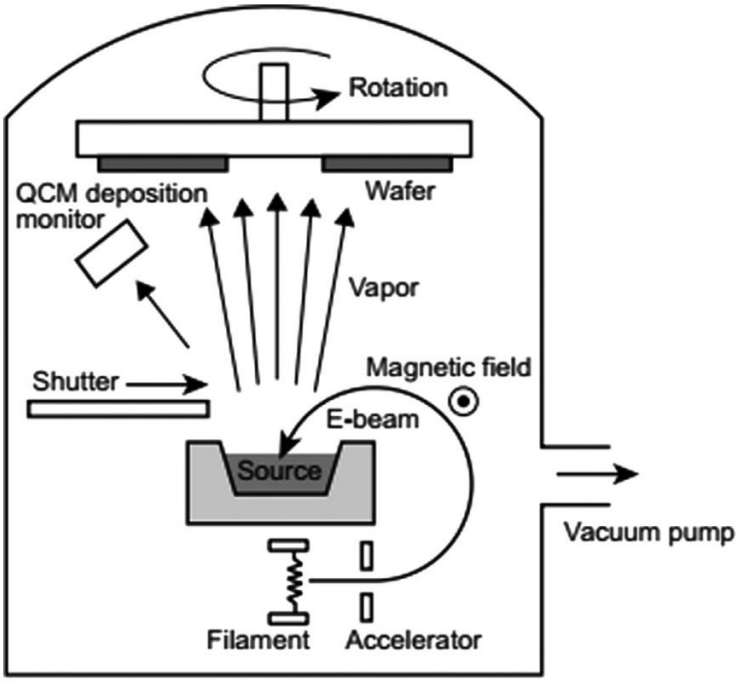

Figure 16 Schematic view of an electron beam evaporation system.[26]

doi:10.6342/NTU202500064

Chapter 3 Experiment and Process Design

3.1 Devices structure view

The figure below shows the top view of our micro-LED design. All the N metal electrodes are designed in a ring shape surrounding the mesa to reduce the current crowding effect. The P metal electrodes, however, have different designs depending on the device size. For the 100μm devices, the electrode is in a "cross" shape, while for the 75μm and 50μm devices, it is in a "plus" shape. Larger devices require bigger electrodes to ensure more uniform current distribution. For devices with sizes ranging from 25μm to 5μm, the electrode covers only a small portion of the mesa to maximize the light-emitting area. For the 3μm devices, the electrode is designed to cover half of the mesa, which helps reduce yield loss due to alignment errors.

doi:10.6342/NTU202500064

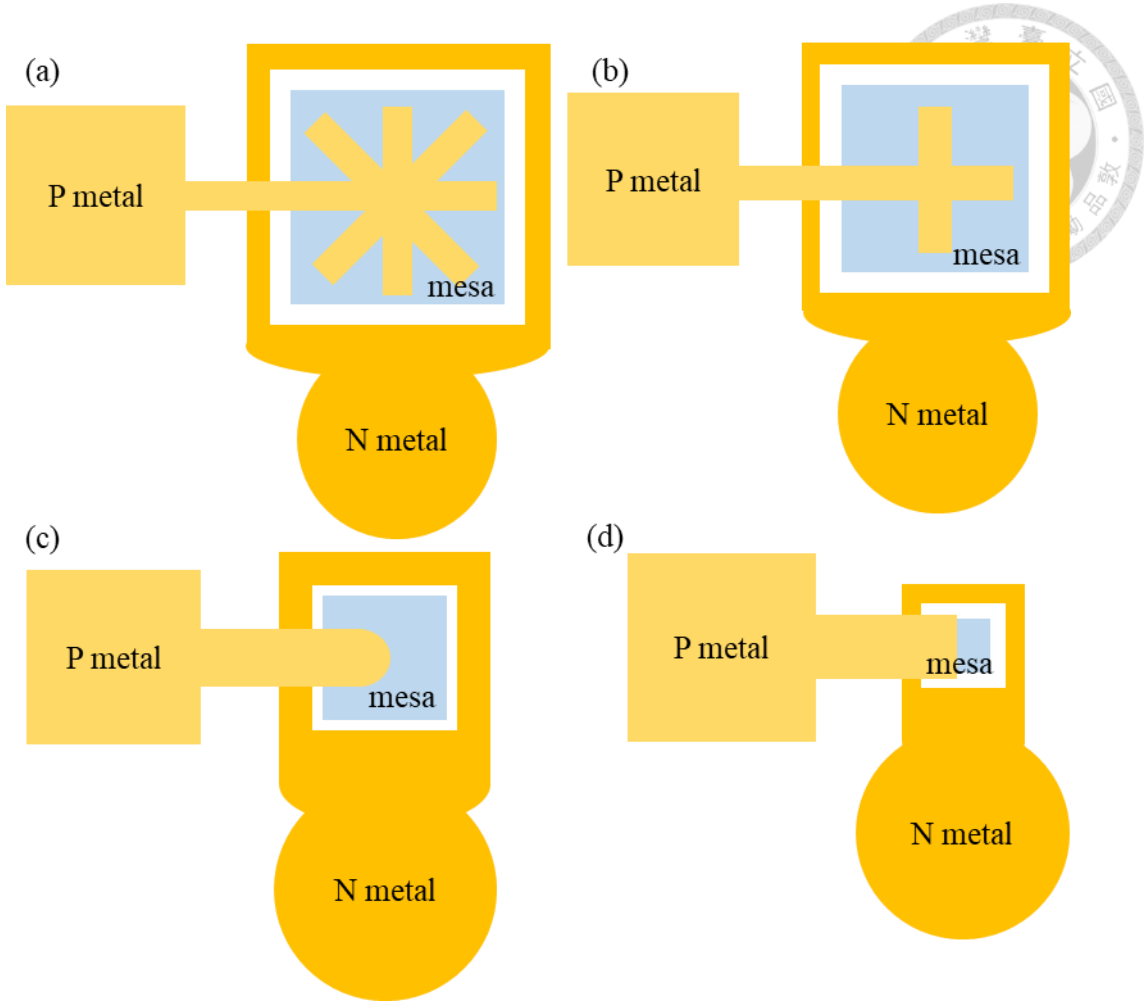

Figure 17 The top view of (a)100μm (b)75μm, 50μm (c)25μm-5μm (d)3μm devices.

3.2 Experiment process flow of micro-LED

Figure 18 shows our process flow, which can be divided into seven steps.

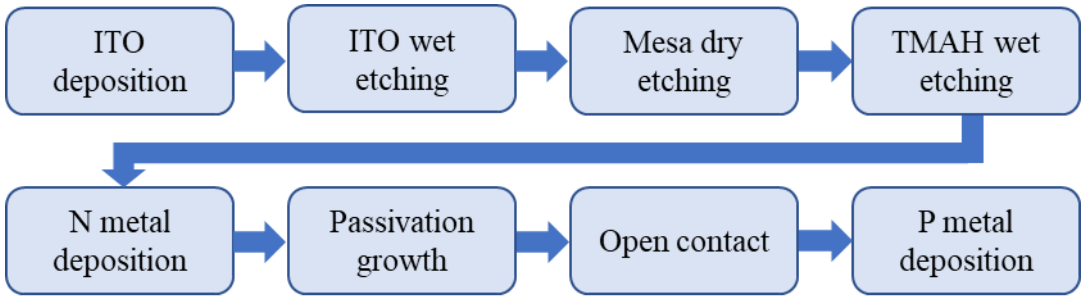

Figure 18 The process flow of micro-LED.

doi:10.6342/NTU202500064

3.2.1 Substrate and epitaxy

We purchase wafers with completed epitaxy from Epileds Technology, Inc. The substrate is Al_2O_3, the p-type layer is AlGaN doped with Mg, the active layer is InGaN/AlGaN with Si, and the n-type layer is AlGaN doped with Si. The peak emission wavelength is between 365nm and 375nm.

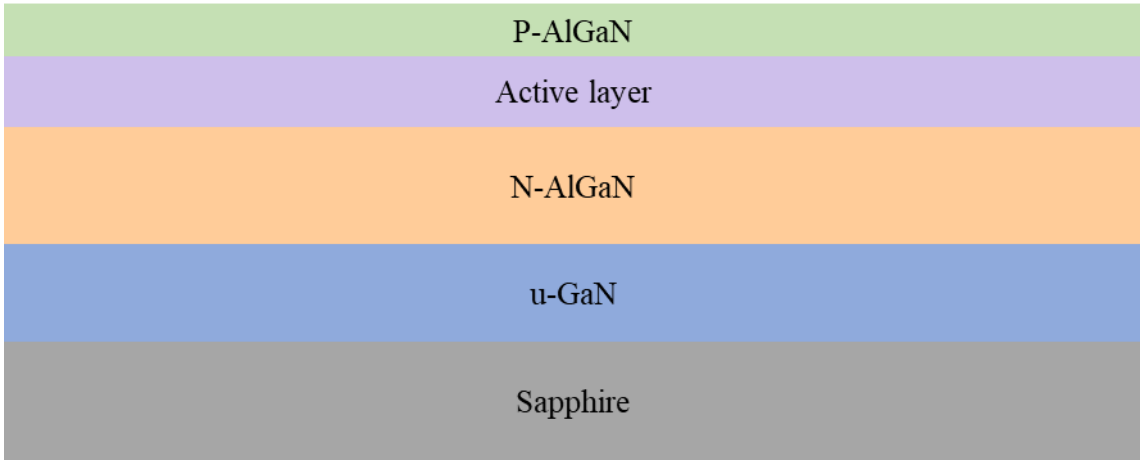

Figure 19 The side view of the epitaxial wafer.

doi:10.6342/NTU202500064

3.2.2 ITO deposition

The first step is to deposit a layer of indium tin oxide (ITO) on the entire wafer using electron beam evaporation, which serves as a transparent current spreading layer. The thickness is approximately 220 nm.

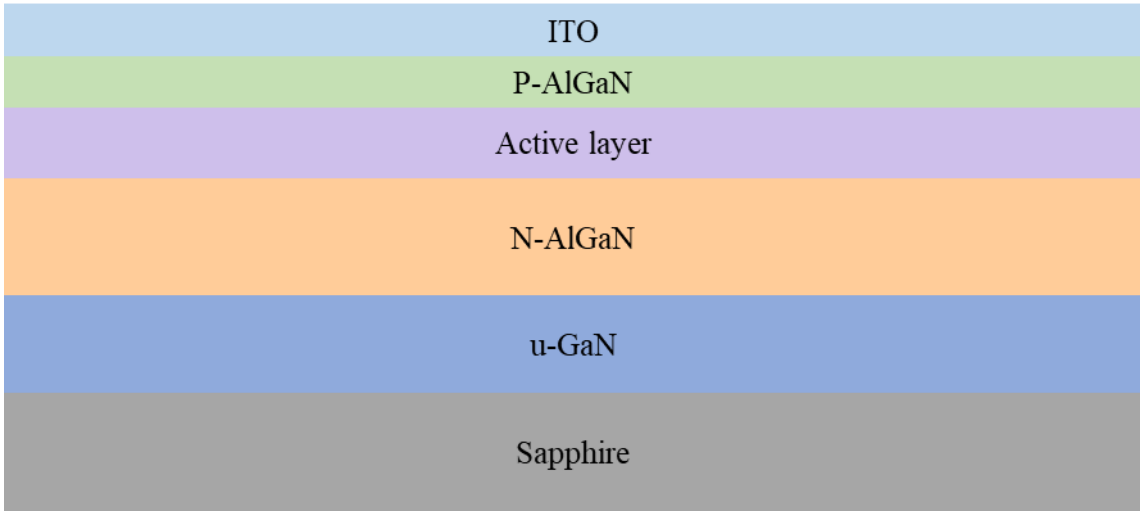

Figure 20 The schematic cross-section view after ITO deposition.

doi:10.6342/NTU202500064

3.2.3 ITO wet etching

A photolithography process is employed to define the mesa, with S1813 selected as the positive photoresist. To etch the ITO layer, we use hydrochloric acid (HCl) as the wet etching solution, maintaining a temperature of 55°C for 2 minutes and 20 seconds.

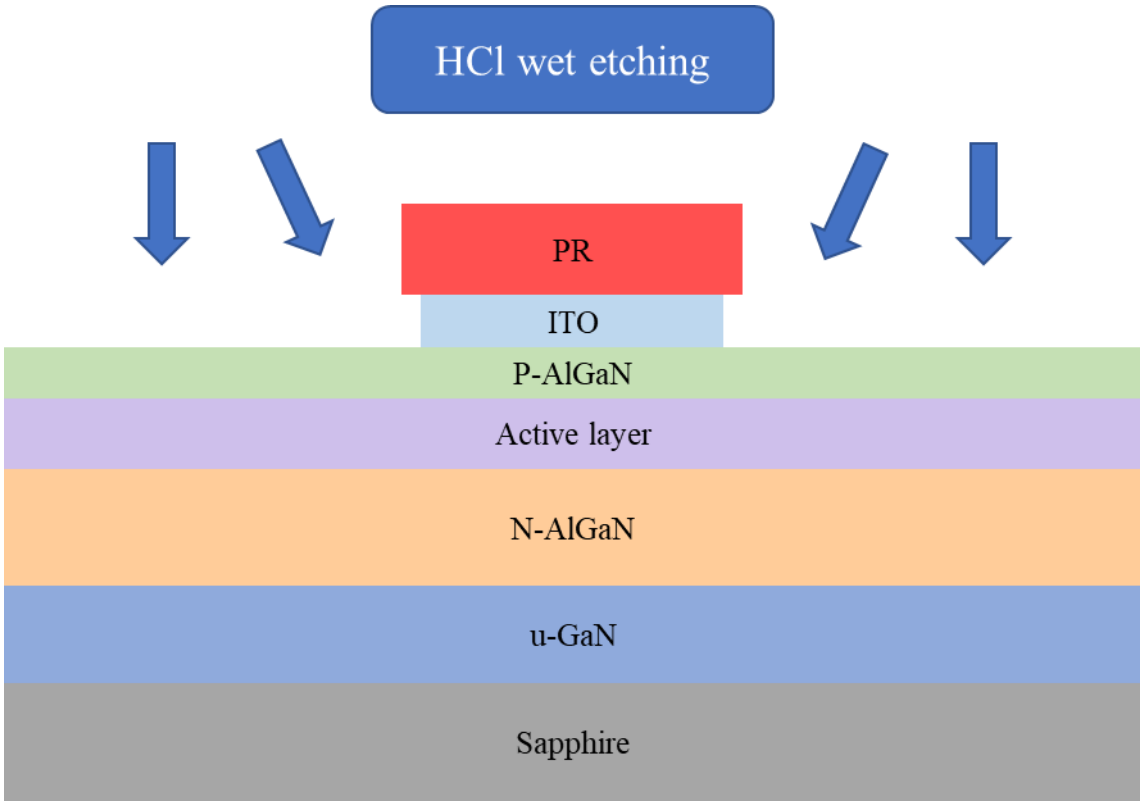

Figure 21 The schematic cross-section view after ITO wet etching.

doi:10.6342/NTU202500064

3.2.4 Mesa dry etching

Mesa dry etching is performed using an inductively coupled plasma (ICP) system with the following parameters: Cl_2 20 sccm, BCl_3 30 sccm, Ar 5 sccm, and RF power of 150 W. A total of two cycles are conducted, with each cycle lasting 100 seconds. The etching depth is approximately 1100 nm.

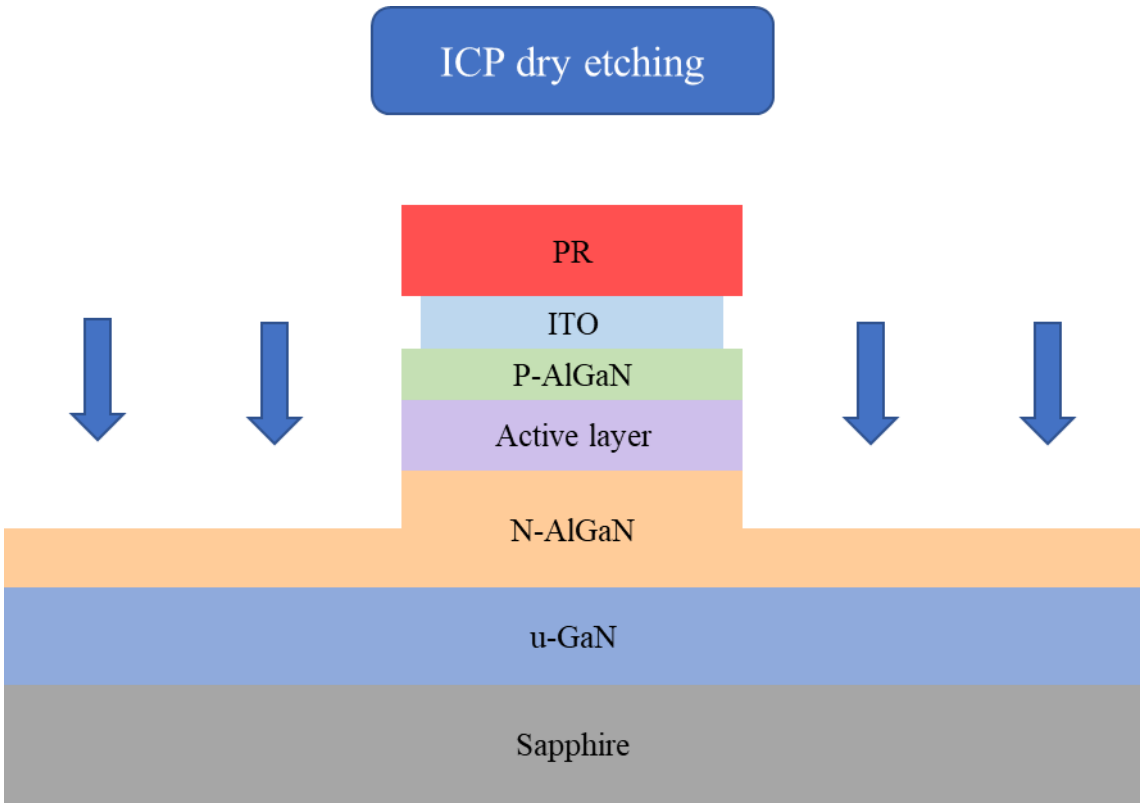

Figure 22 The schematic cross-section view after mesa dry etching.

doi:10.6342/NTU202500064

3.2.5 TMAH wet etching

Typically, after ICP etching, the sidewalls of the mesa are rough and contain many defects. Therefore, we perform a tetramethylammonium hydroxide (TMAH) wet etch on the sidewalls. The TMAH treatment helps to eliminate etching damage and flattens the sidewalls surfaces.[27] After this step, the photoresist is removed by acetone.

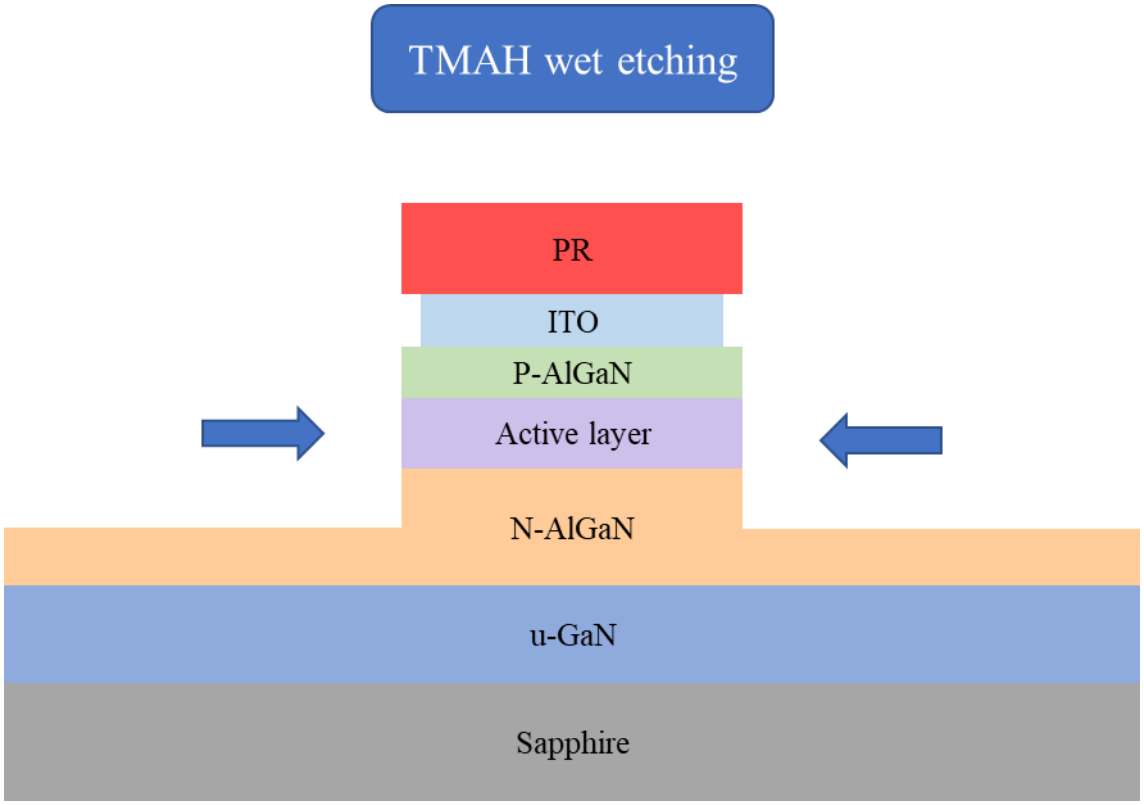

Figure 23 The schematic cross-section view of TMAH treatment.

doi:10.6342/NTU202500064

3.2.6 N metal deposition

We use an E-beam evaporator to deposit N metal, with 30 nm of chromium and 200 nm of gold. We choose AZ5214 as the photoresist, which is originally a positive photoresist. After a post-exposure bake and a flood exposure, it transforms into a negative photoresist. The characteristics of the negative photoresist are suitable for metal deposition because it easily forms an undercut, which facilitates a smoother lift-off process. When depositing metal, it is important to ensure that the deposition rate is not too fast, as this could lead to poor contact. Additionally, the temperature inside the chamber should be carefully monitored, as excessively high temperatures may cause the photoresist to harden, making the lift-off process more difficult.

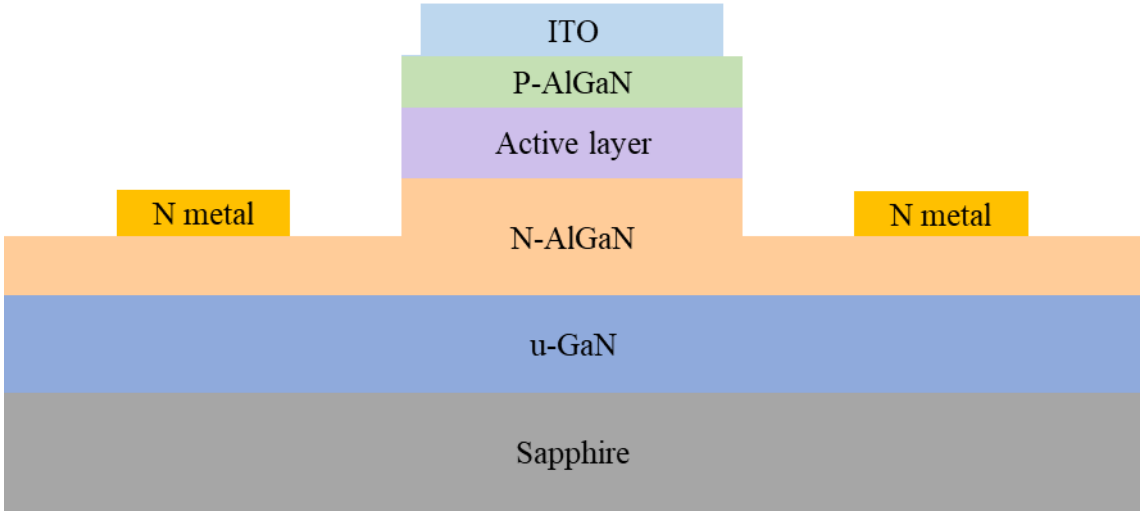

Figure 24 The schematic cross-section view after N metal deposition.

doi:10.6342/NTU202500064

3.2.7 Passivation layer deposition

Next, we use Plasma Enhanced Chemical Vapor Deposition (PECVD) to deposit an insulating layer of silicon dioxide (SiO_2), approximately 300 nm thick. This layer serves to electrically isolate the P and N metals, preventing short circuits of the devices.

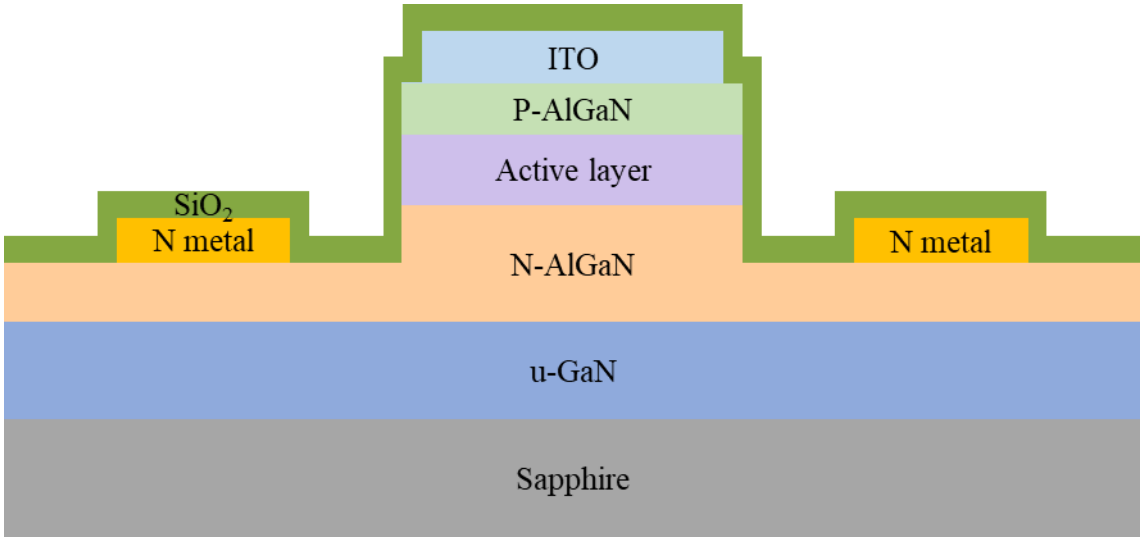

Figure 25 The schematic cross-section view after SiO_2 deposition.

doi:10.6342/NTU202500064

3.2.8 Open contact

After the deposition of the insulating layer, we need to open up part of the passivation layer, specifically in the central region of the mesa, to allow the subsequent P metal to make contact with the ITO layer. Additionally, we need to open areas for the N metal contact points.

In this step, we use Reactive Ion Etching (RIE) dry etching instead of Buffered Oxide Etch (BOE) wet etching. This approach is chosen to better control the etching process and avoid the isotropic etching that could lead to potential short circuits.

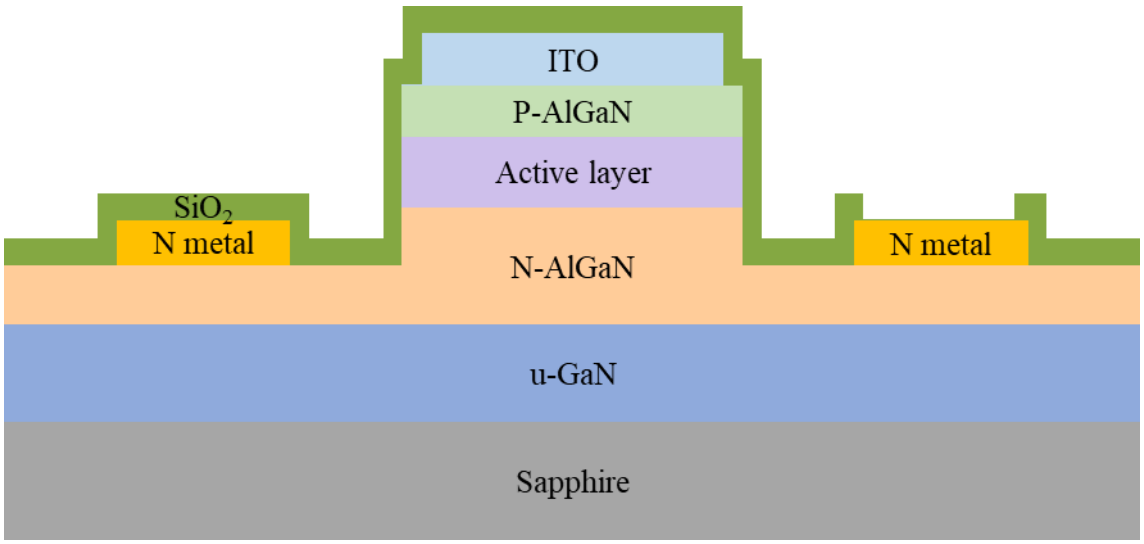

Figure 26 The schematic cross-section view after open contact.

doi:10.6342/NTU202500064

3.2.9 P metal deposition

The final step is P metal plating, where we use E-beam deposition to deposit 30nm of Nickel and 200nm of Gold.

Based on the different mesa sizes, we have designed four different P metal patterns. The larger devices use cross-shaped and "X"-shaped patterns, while the smaller devices have elongated patterns. The smallest, with a 3μm size, is designed to cover half of the mesa.

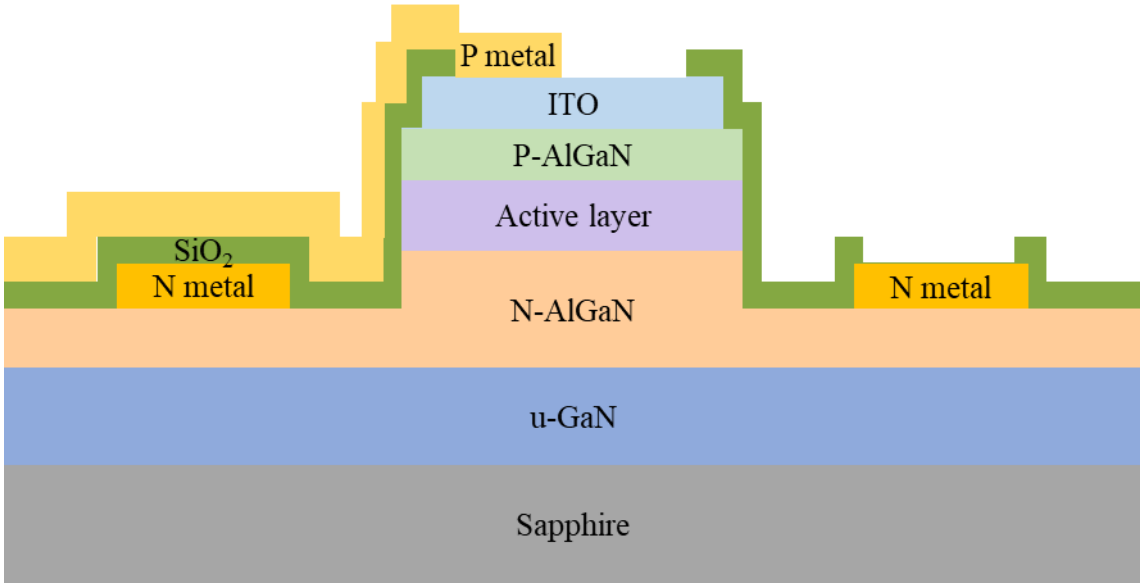

Figure 27 The schematic cross-section view after P metal deposition.

doi:10.6342/NTU202500064

Chapter 4 Results and Discussion

4.1 Electrical properties

We first measure the IV characteristics of the devices, ranging from -20V to 5V, including various sizes and two different fabrication methods (with TMAH treatment and without TMAH treatment). Then, we analyze parameters such as leakage current, ideality factor, and series resistance using the IV data.

4.1.1 JV characteristics

To better compare the IV characteristics between different sizes, we convert the current (I) into current density (J) to plot the forward bias region. **Figure 28** and **Figure 29** show the JV curves for devices with TMAH treatment and without TMAH treatment, respectively.

We can observe that in devices with TMAH treatment, the devices exhibit better regularity. Under the same voltage, smaller devices have higher current density, which means that for smaller devices, we can achieve the same current density with a lower voltage. In devices without TMAH treatment, however, this phenomenon is not observed.

doi:10.6342/NTU202500064

The lack of sidewall treatment leads to instability in the device's electrical characteristics.

A detailed comparison of the IV characteristics will be presented later.

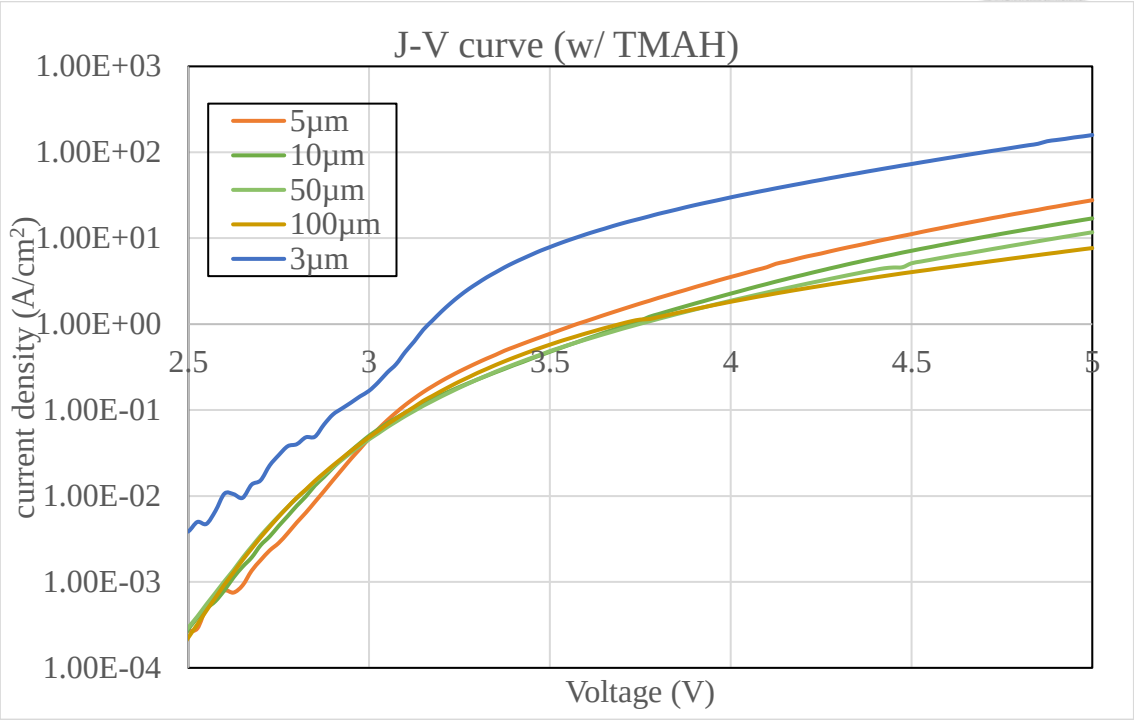

Figure 28 J-V characteristic of different sizes of micro-LED (w/ TMAH).

doi:10.6342/NTU202500064

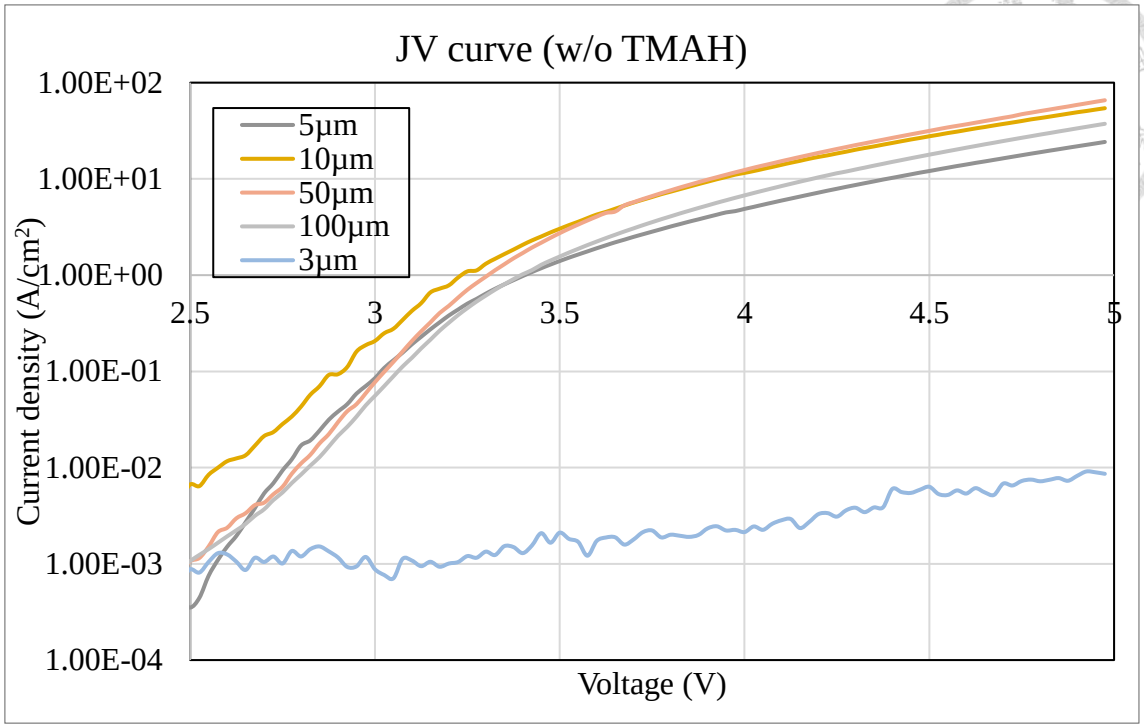

Figure 29 J-V characteristic of different sizes of micro-LED (w/o TMAH).

4.1.2 IV characteristics

Next, we use the IV curve to compare the impact of TMAH treatment on the electrical properties of devices with different sizes.

We can observe that under negative bias, regardless of the device size, the TMAH treated devices bear lower leakage than the un-treated ones. In fact, some devices with TMAH treatment exhibit leakage currents so low that they are undetectable due to the limitations of the measurement equipment. In the positive bias region, due to the leakage current,

doi:10.6342/NTU202500064

devices without TMAH treatment will turn on earlier than the TMAH treated ones. The most noticeable difference here is seen in the 3x3 μm² device. The 3 μm micro-LED without TMAH treatment not only has a higher leakage current, but it also fails to operate like a normal diode. Instead, it behaves more like a resistor.

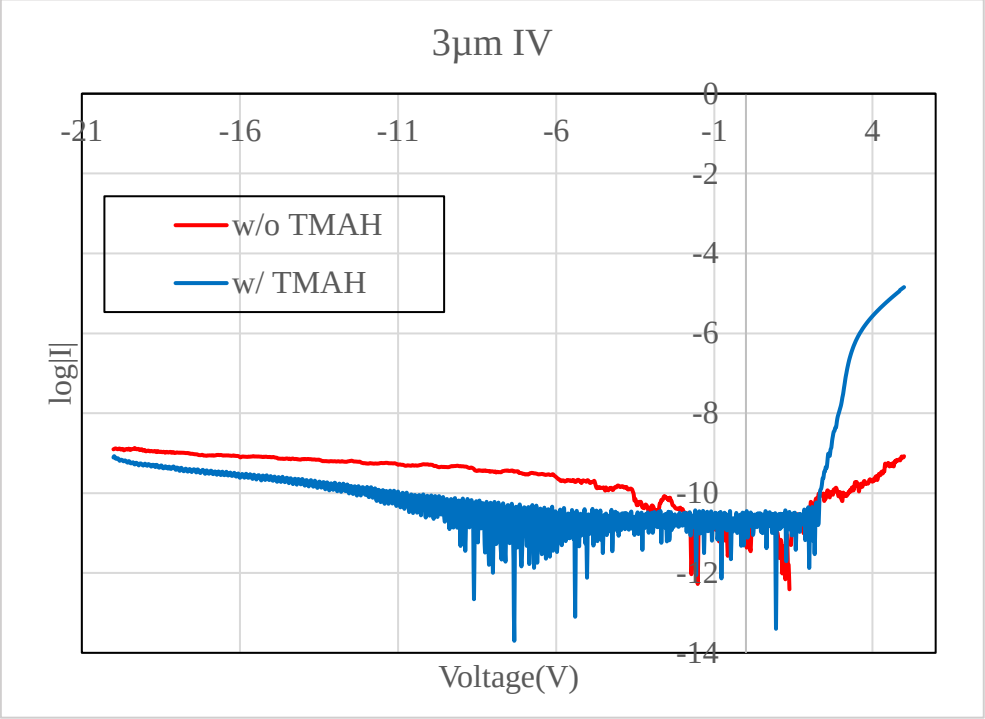

Figure 30 IV curve of the 3μm devices.

doi:10.6342/NTU202500064

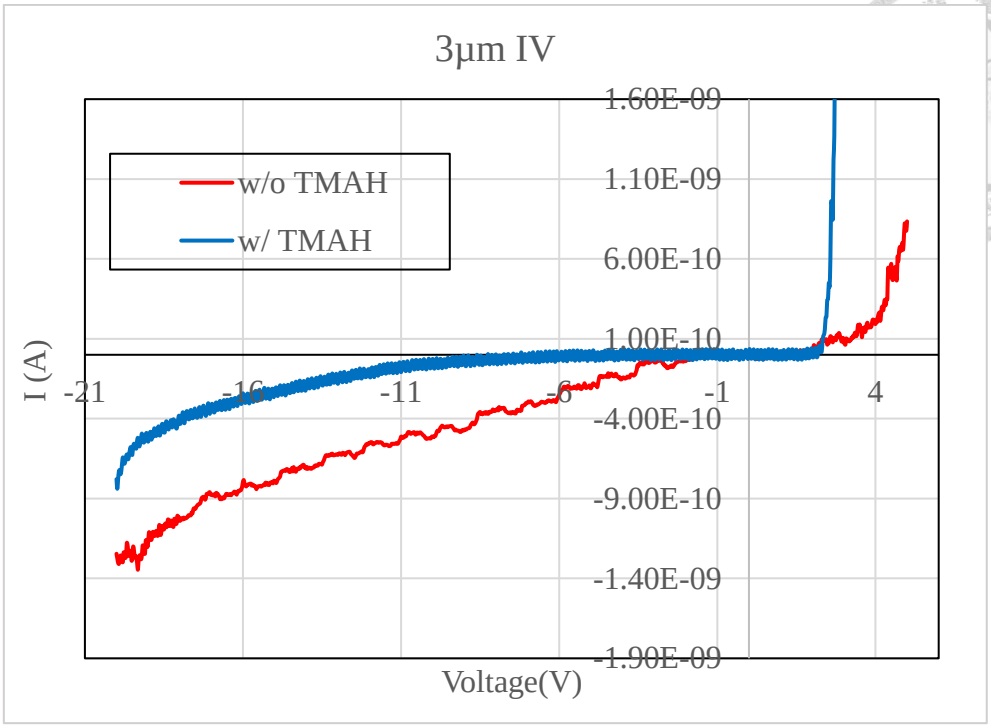

Figure 31 IV curve of the 3μm devices (linear scale).

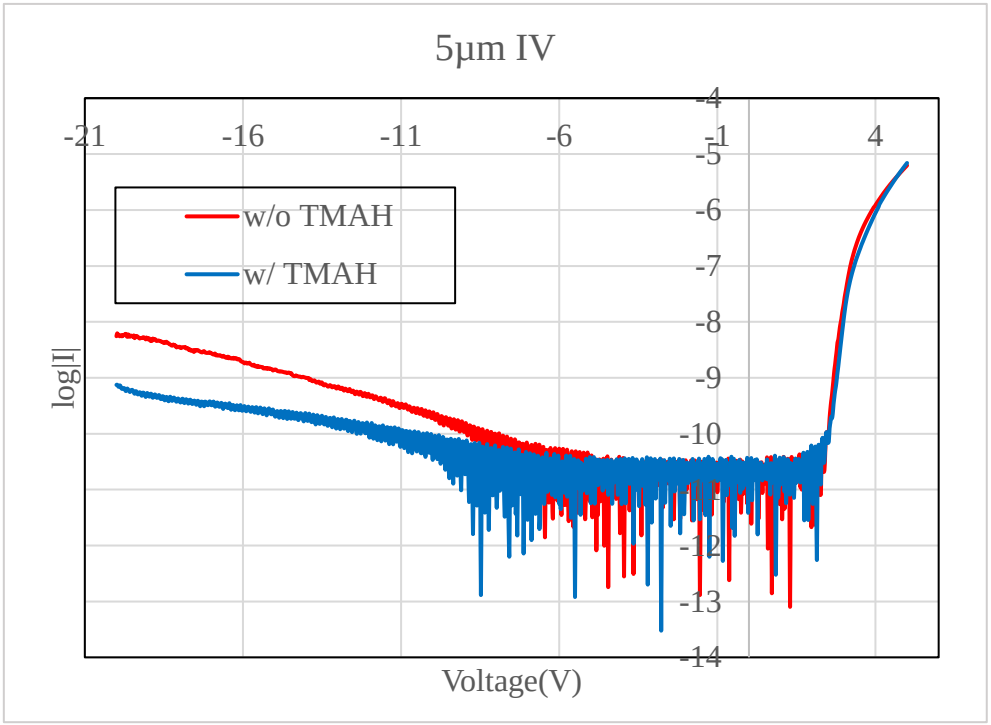

Figure 32 IV curve of the 5μm devices.

doi:10.6342/NTU202500064

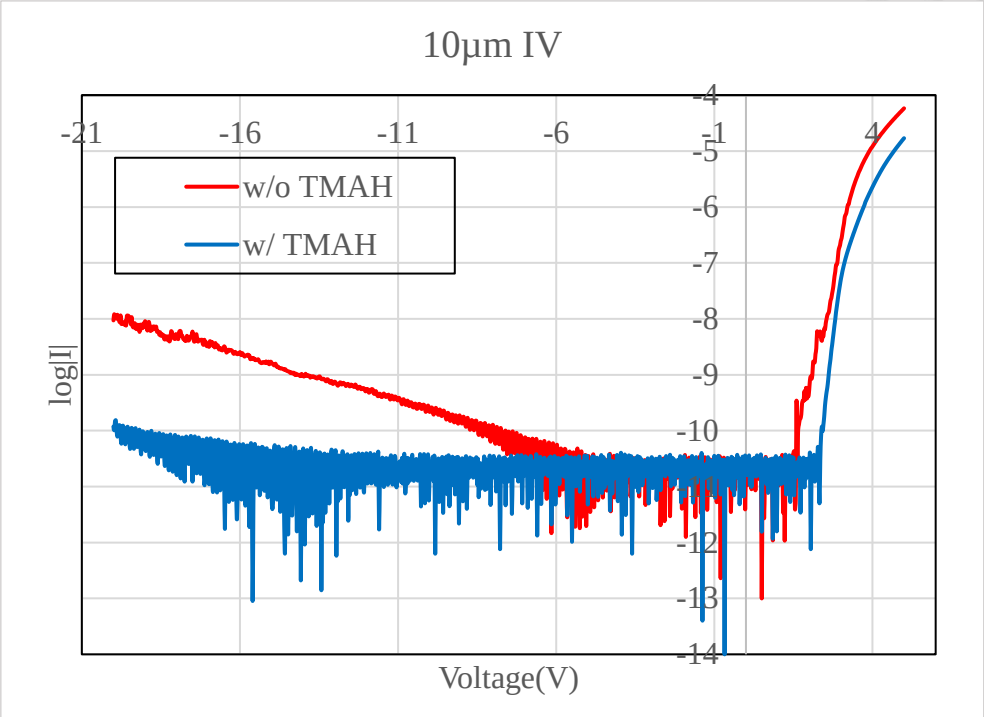

Figure 33 IV curve of the 10μm devices.

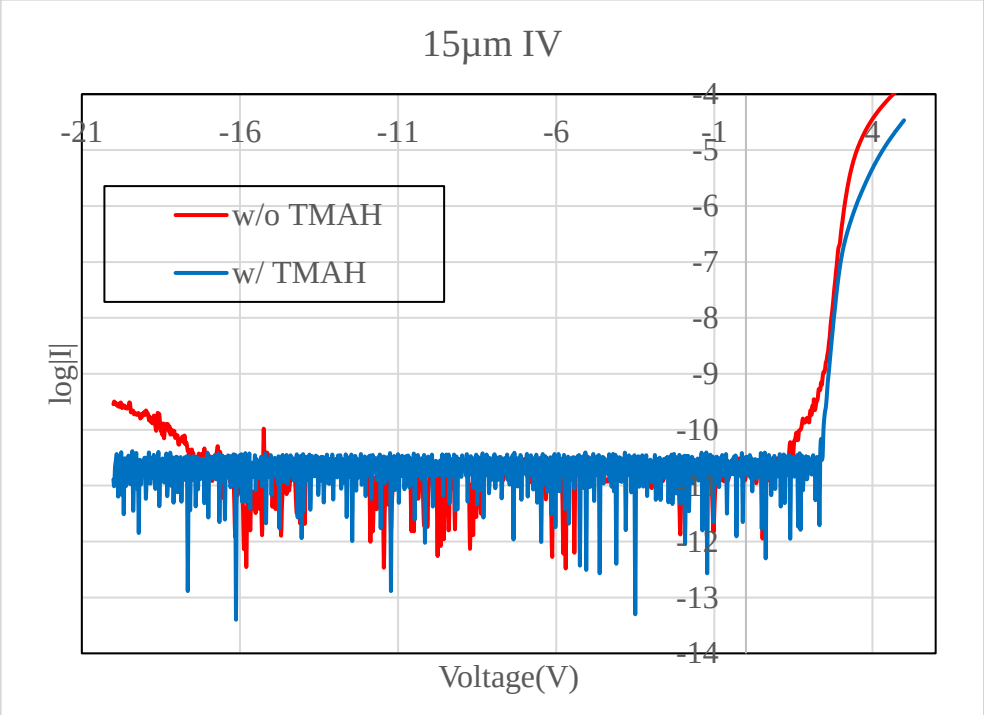

Figure 34 IV curve of the 15μm devices.

doi:10.6342/NTU202500064

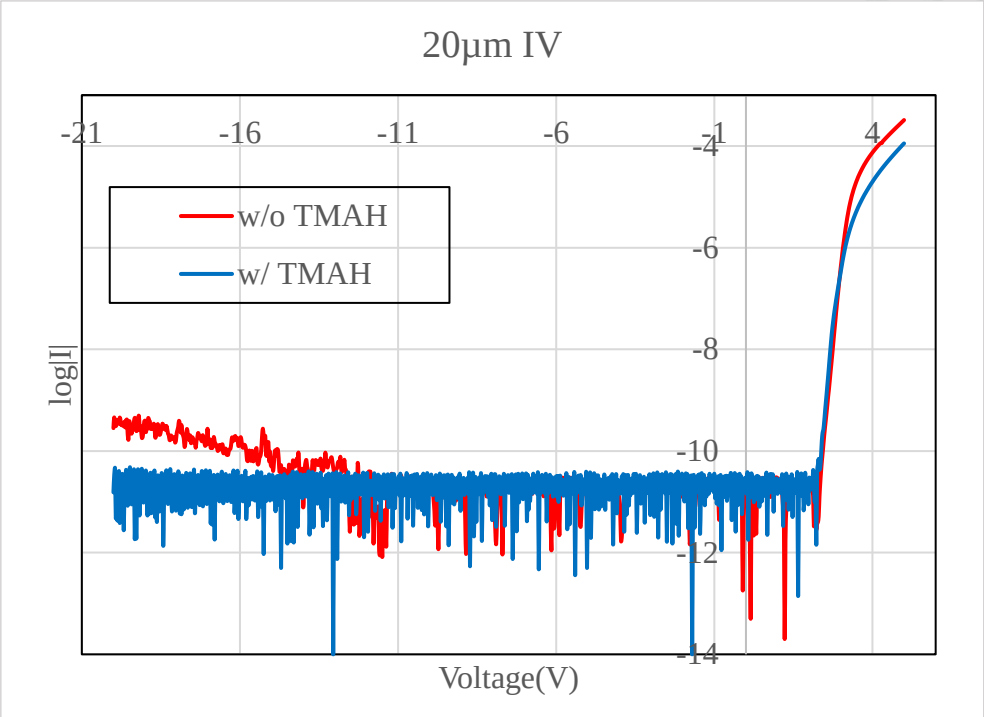

Figure 35 IV curve of the 20μm devices.

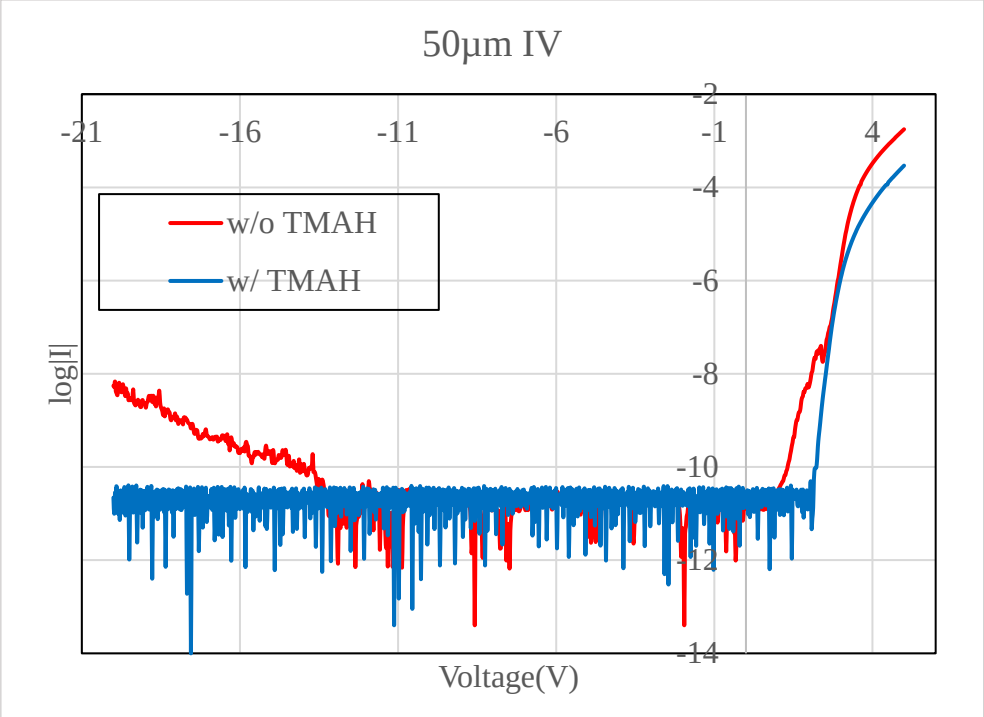

Figure 36 IV curve of the 50μm devices.

doi:10.6342/NTU202500064

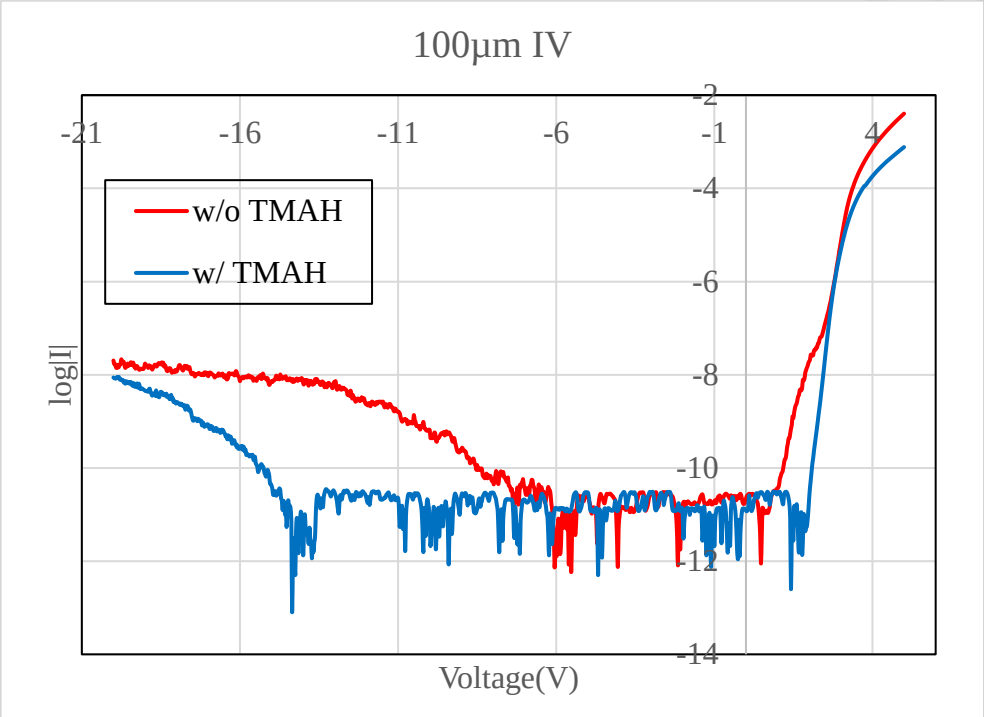

Figure 37 IV curve of the 100μm devices.

4.1.3 Leakage current

Here, we can determine the leakage current of each device at -20V from the IV characteristics. From the graph, we can see that the leakage current of devices without TMAH treatment, from smaller to larger sizes, are 1.28E-09A, 5.80E-09A, 1.07E-08A, 2.96E-10A, 3.48E-10A, 5.13E-09A, and 1.66E-08A. The leakage currents of TMAH-treated devices are smaller than those of untreated ones in all sizes, with values of 7.70E-10A, 7.25E-10A, 1.24E-10A, 8.99E-12A, 1.05E-11A, 9.22E-12A, and 8.53E-09A. For

doi:10.6342/NTU202500064

the 15μm, 20μm, and 50μm TMAH-treated devices, we were unable to measure the correct leakage currents due to the limitations of the equipment.

During the dry etching process of the mesa, damage to the chip's sidewalls may occur. As sidewall defects become more pronounced, the leakage current increases. TMAH treatment can effectively flatten and smooth the sidewall morphology, resulting in a reduction in leakage current.

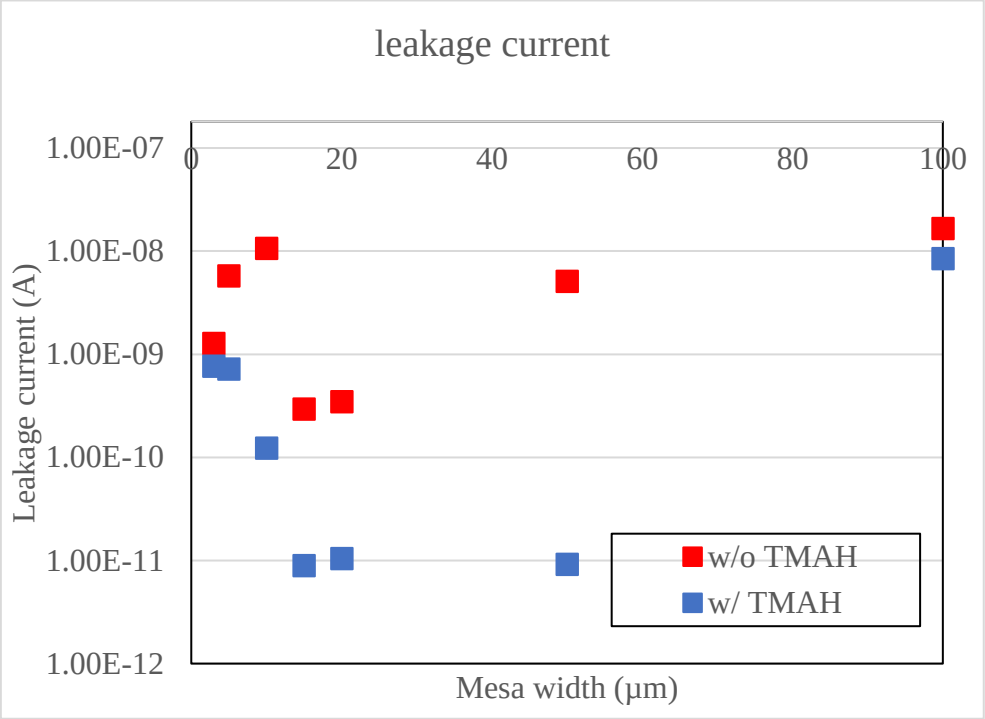

Figure 38 The comparison of the leakage current at -20V.

doi:10.6342/NTU202500064

	w/o TMAH	w/ TMAH
3μm	1.28E-09	7.70E-10
5μm	5.80E-09	7.25E-10
10μm	1.07E-08	1.24E-10
15μm	2.96E-10	8.99E-12
20μm	3.48E-10	1.05E-11
50μm	5.13E-09	9.22E-12
100μm	1.66E-08	8.53E-09

Table 1 The comparison of the leakage current at -20V.

4.1.4 Ideality factor

The current-voltage relationship of a diode can be expressed by the following equation:

$$I_D = I_S(e^{\frac{qV_D}{nkT}} - 1) \qquad \textbf{Equation 1}$$

In this equation, I_D, and V_D represent the diode current and voltage, respectively, I_S is the saturation current, q is the elementary charge, k is the Boltzmann constant, T is the temperature, and n is the ideality factor, which is the focus of this discussion.

doi:10.6342/NTU202500064

Through the calculation of the I-V curve, we determine the ideality factor n for each device. According to the Sah-Noyce-Shockley (SNS) analysis, the ideality factor n should be between 1 and 2.[28] However, the n values calculated for our devices are all greater than 2. This discrepancy arises because, during the calculation, we cannot ignore the effects of the metal contact and the internal heterojunctions on the IV characteristics.[29] As a result, the calculated ideality factor is inconsistent with the SNS analysis. Nonetheless, we can still observe that, in the comparison between devices with TMAH treatment and those without, the treated devices have a smaller ideality factor, which is closer to that of an ideal diode.

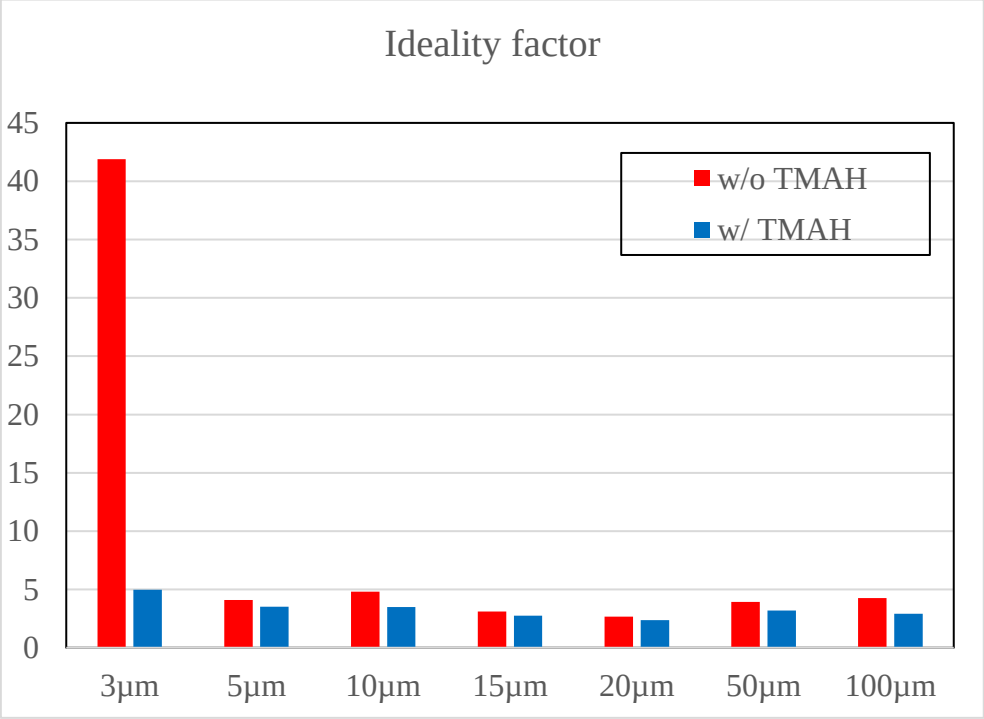

Figure 39 The comparison of the ideality factor.

doi:10.6342/NTU202500064

	w/o TMAH	w/ TMAH
3μm	41.89756	4.972874
5μm	4.109716	3.521678
10μm	4.809657	3.492236
15μm	3.103436	2.764692
20μm	2.65628	2.354982
50μm	3.940609	3.191451
100μm	4.260818	2.926487

Table 2 The comparison of the ideality factor.

4.1.5 Series resistant

We can also calculate the device's series resistance R_s through the I-V curve. We first observe that the smaller the device, the larger the series resistance. This is because the metal-semiconductor contact in smaller devices tends to be worse than in larger devices. Additionally, the result we obtained shows that the series resistance of TMAH-treated devices is higher than that of the untreated ones. This result is consistent with the study on diodes by M. Siva Pratap Reddy et al.[30] The cause of this result could be that TMAH

doi:10.6342/NTU202500064

etching damages the n-GaN[31], leading to poor contact between the N metal and the n-type material, which increases the series resistance.

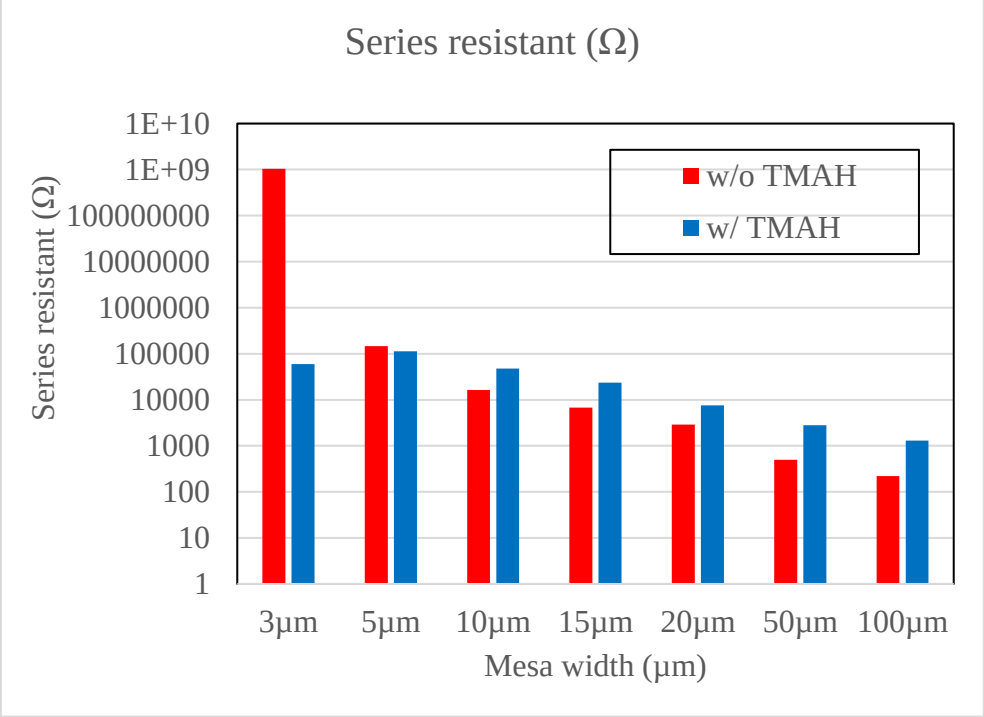

Figure 40 The comparison of the series resistant.

doi:10.6342/NTU202500064

	w/o TMAH	w/ TMAH
3μm	1.033E+09	59343.82
5μm	145921.41	113335.8
10μm	16219.696	47553.4
15μm	6774.6979	23421
20μm	2893.3372	7609.536
50μm	494.9778	2824.793
100μm	219.41006	1294.747

Table 3 The comparison of the series resistant.

4.2 External Quantum Efficiency (EQE)

External Quantum Efficiency (EQE) is defined as the ratio of the number of charge carriers (electrons or holes) converted into emitted photons from the LED device. It can be divided into two components: Light Extraction Efficiency (LEE) and Internal Quantum Efficiency (IQE). LEE refers to the proportion of photons generated in the

doi:10.6342/NTU202500064

active layer that are emitted outside the device. IQE refers to the proportion of injected charge carriers that are converted into photons.

The relationship between these components can be expressed by the following equation:

$$EQE = LEE \times IQE$$
$$= \frac{Number\ of\ photons\ emitted\ outside}{Number\ of\ photons\ generated} \times \frac{Number\ of\ photons\ generated}{Number\ of\ injected\ charge\ carriers}$$
$$= \frac{Number\ of\ photons\ emitted\ outside}{Number\ of\ injected\ charge\ carriers}$$

In the experimental process, we use a photodetector (PD) to measure the photocurrent. Then, through the PD's Incident Photon-Electron Conversion Efficiency (IPCE), we convert the number of electrons into the number of photons. Finally, by dividing this number by the number of electrons injected into the device, we can calculate the External Quantum Efficiency (EQE)**.**

$$EQE = \frac{I_{PD}/IPCE/e}{I_{supplied}/e} \qquad \textbf{Equation 2}$$

The IQE of an LED can be analyzed using the ABC model, and therefore, the behavior of EQE can also be explained using this model.

doi:10.6342/NTU202500064

$$EQE = LEE \times \frac{Bn^2}{An + Bn^2 + Cn^3}$$ **Equation 3**

In **Equation 3**, n represents the injected carriers into the device, A is the Shockley-Read-Hall (SRH) non-radiative recombination coefficient, B is the radiative recombination coefficient, and C is the Auger recombination coefficient. Among these, only B represents the coefficient for the radiative (light-emitting) process.

The coefficient A can be significantly affected by sidewall damage. Therefore, the ratio of the perimeter to the area of the device, which changes with the size of the device, also contributes to the difference in EQE. For smaller devices, the sidewall area makes up a larger proportion of the total device volume, so the sidewall damage has a greater impact on the SRH coefficient A, leading to a lower EQE compared to larger devices. This result can be seen from the study by D. Anis et al.[32], where the EQE of the micro-LED increases as the mesa size increases, as shown in **Figure 41**.

Our experimental data also supports this phenomenon, as both TMAH-treated devices and untreated ones follow this trend. However, the results for larger devices seem somewhat inconsistent, which could be due to several factors. One possibility is that the P-metal of the larger devices may block some of the emitted light due to the design. Another potential reason could be that the size of the photodetector is not large enough

doi:10.6342/NTU202500064

to capture all the light emitted by the LED, leading to an inaccurate measurement of EQE for the larger devices, and thus, the EQE trend for the larger devices does not align with the expected results.

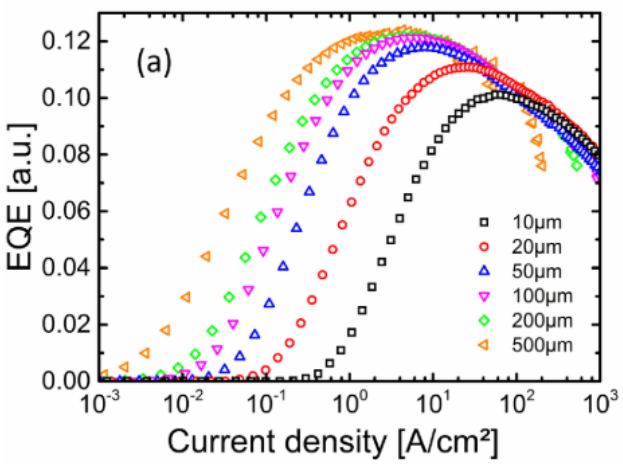

Figure 41 EQE versus current density for different LED sizes[32]

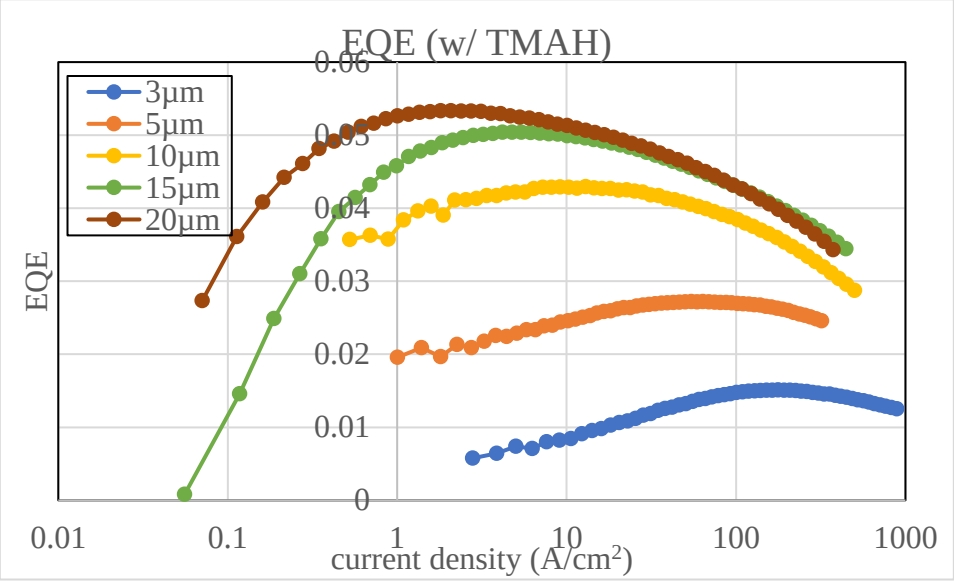

Figure 42 EQE with TMAH treatment for small devices.

doi:10.6342/NTU202500064

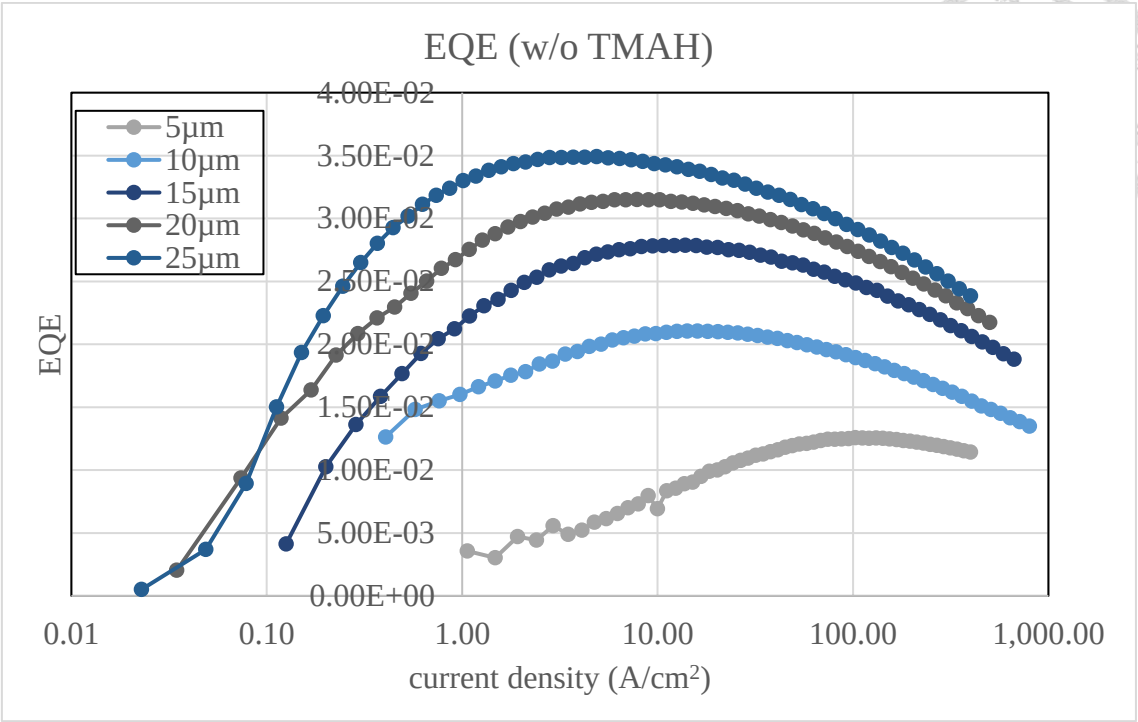

Figure 43 EQE without TMAH treatment for small devices.

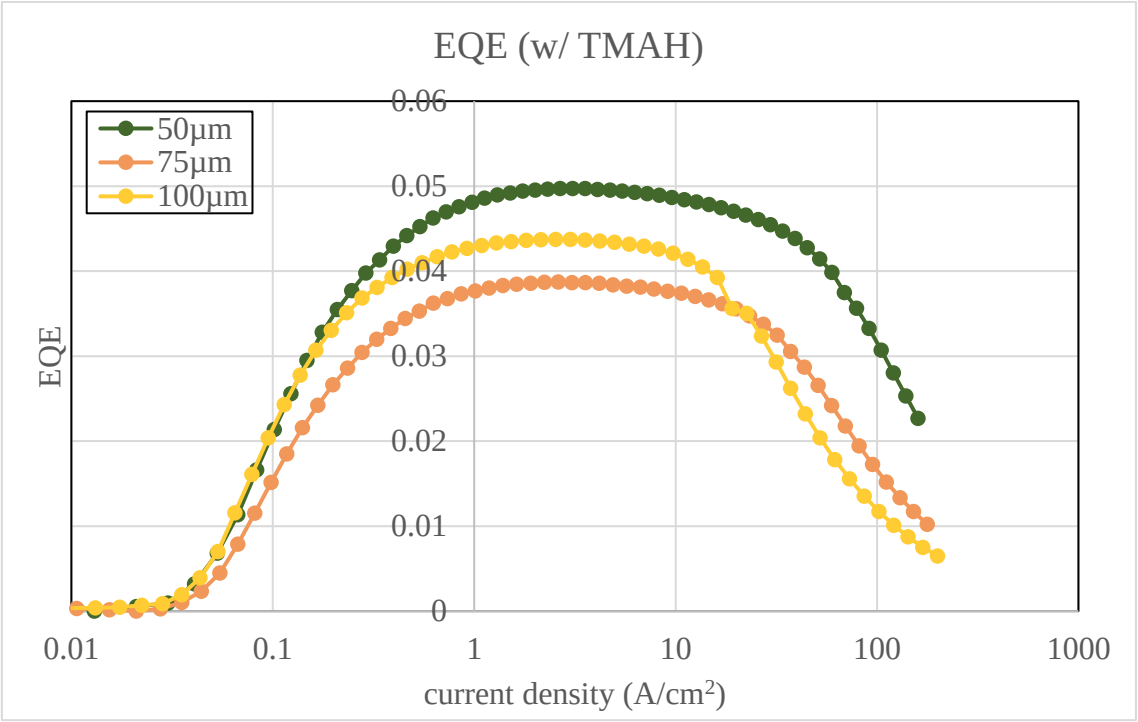

Figure 44 EQE with TMAH treatment for large devices.

doi:10.6342/NTU202500064

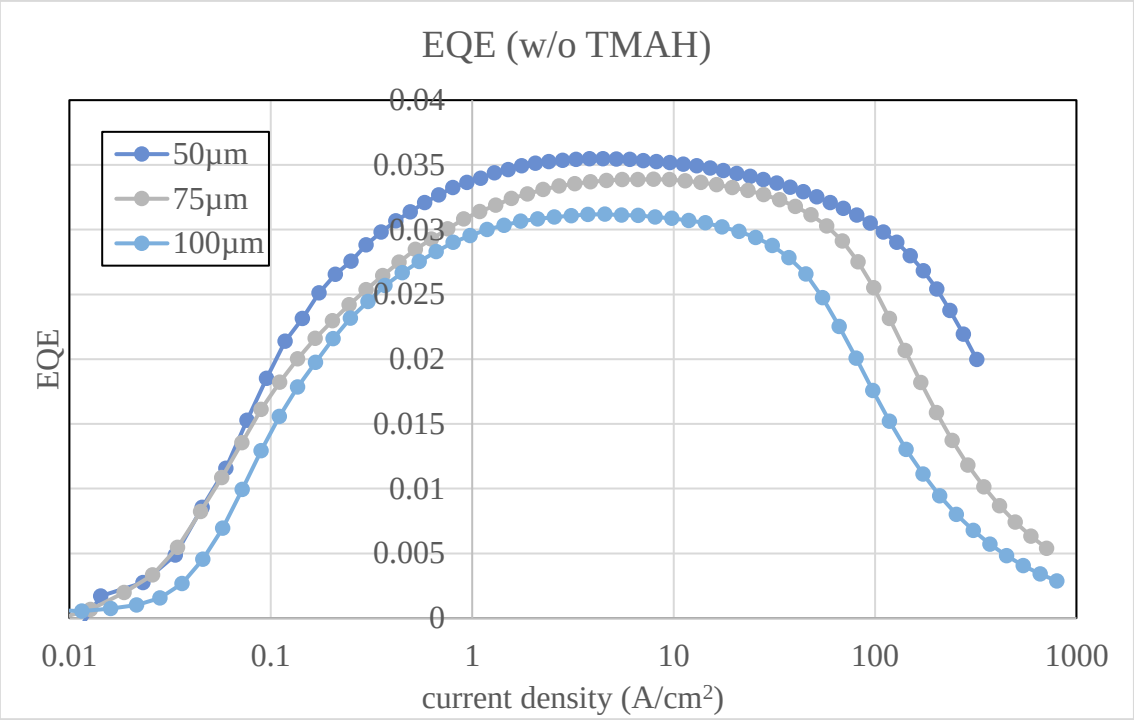

Figure 45 EQE without TMAH treatment for large devices.

Next, we compare devices of the same size. It can be observed that for each device size, the TMAH-treated devices have a higher EQE than the untreated ones. This is because TMAH treatment effectively mitigates the impact of sidewall damage, which helps reduce the SRH non-radiative recombination coefficient A, thereby improving the EQE. Notably, for the 3μm devices, only the ones with TMAH treatment exhibit normal light emission.

doi:10.6342/NTU202500064

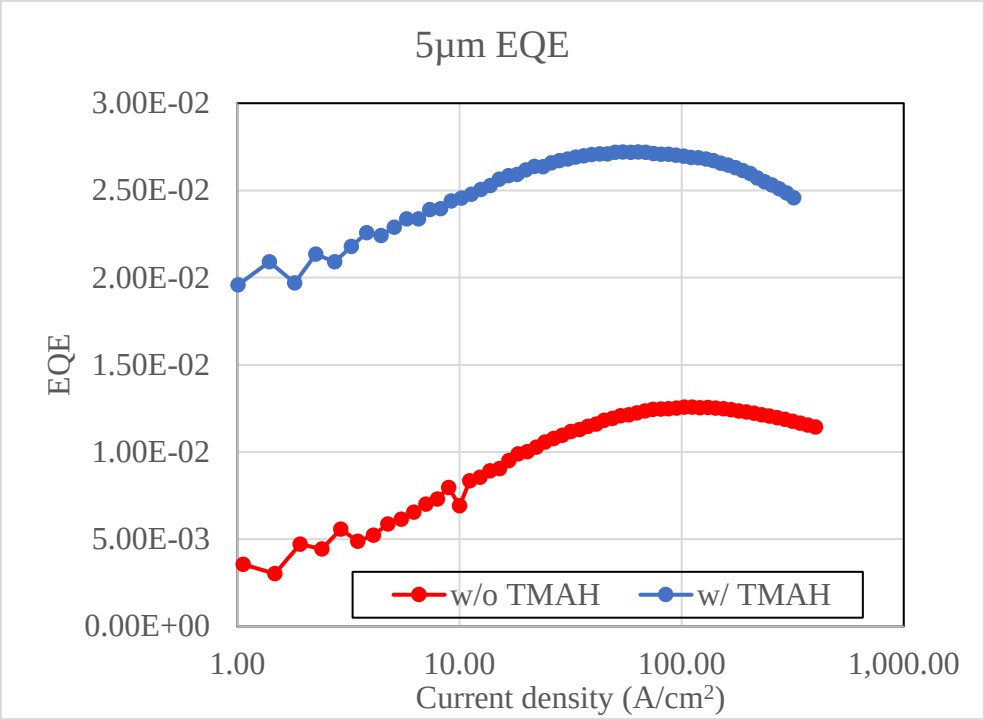

Figure 46 EQE comparison of 5x5μm^2 devices.

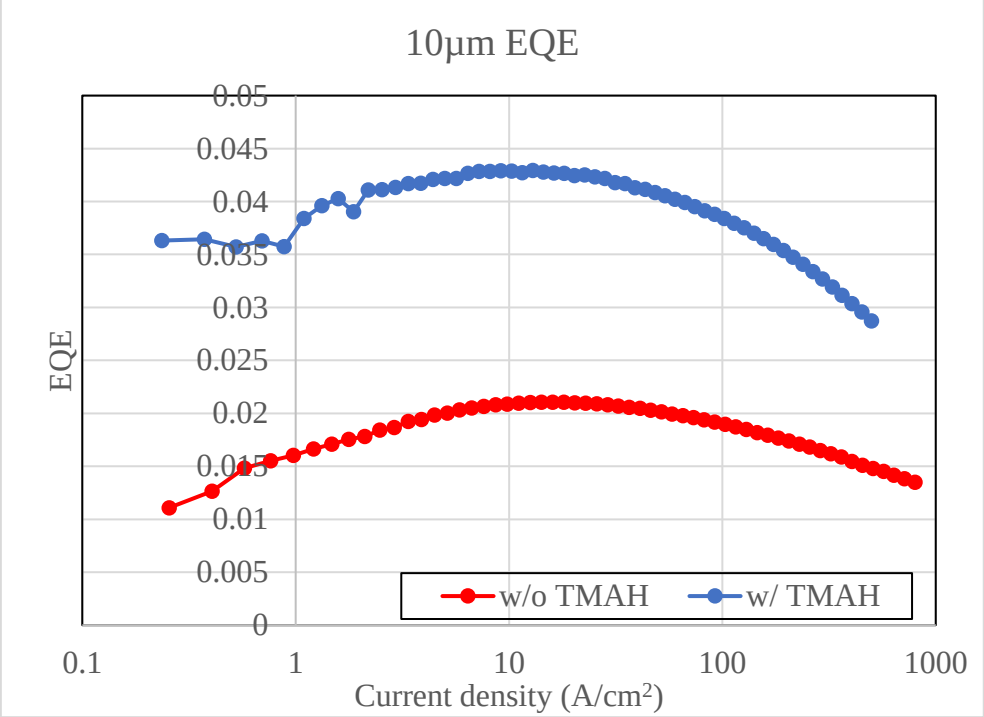

Figure 47 EQE comparison of 10x10μm^2 devices.

doi:10.6342/NTU202500064

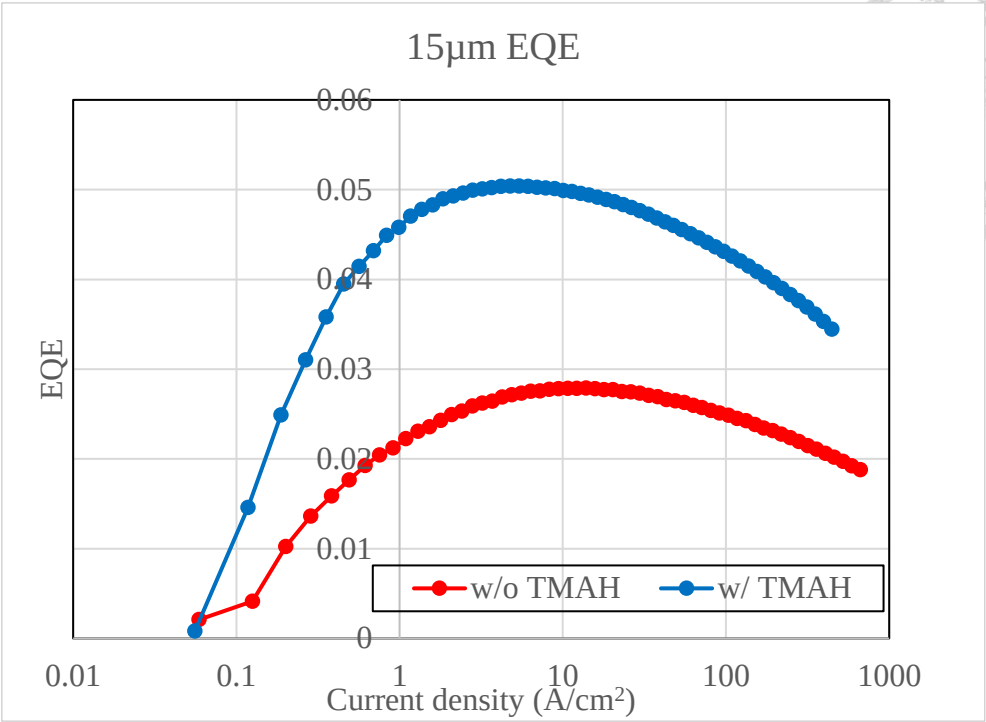

Figure 48 EQE comparison of 15x15μm^2 devices.

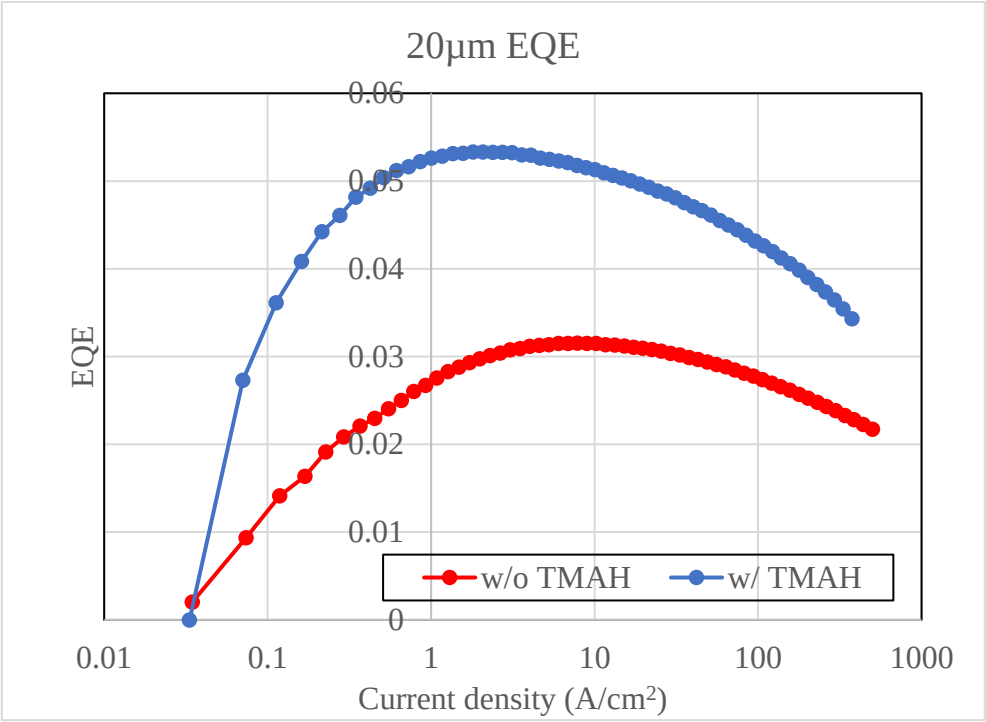

Figure 49 EQE comparison of 20x20μm^2 devices.

doi:10.6342/NTU202500064

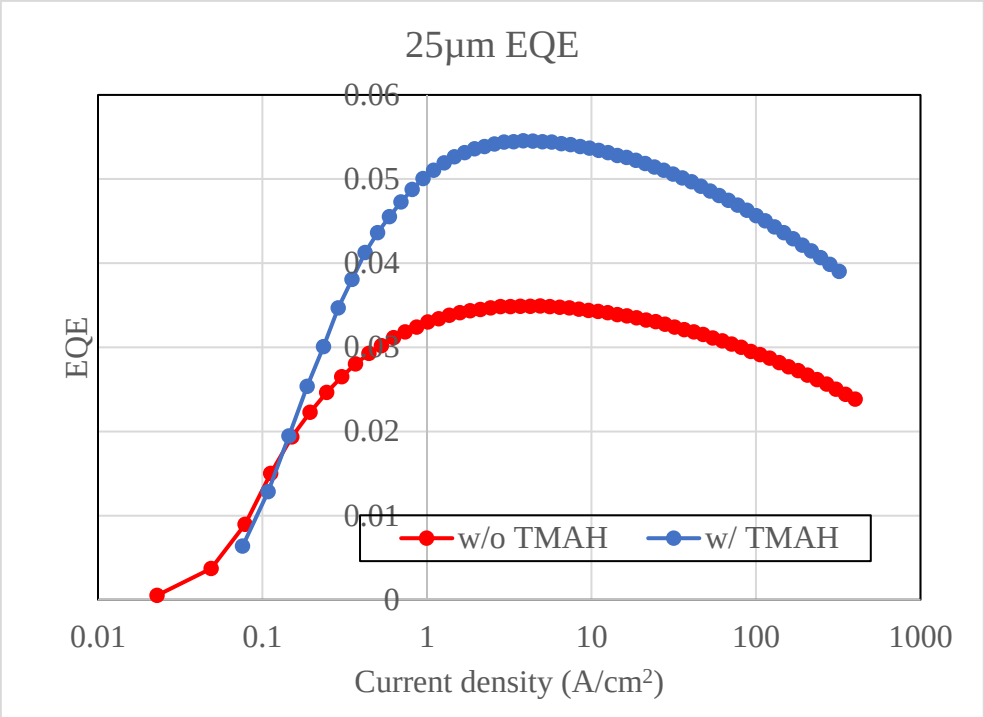

Figure 50 EQE comparison of 25x25μm^2 devices.

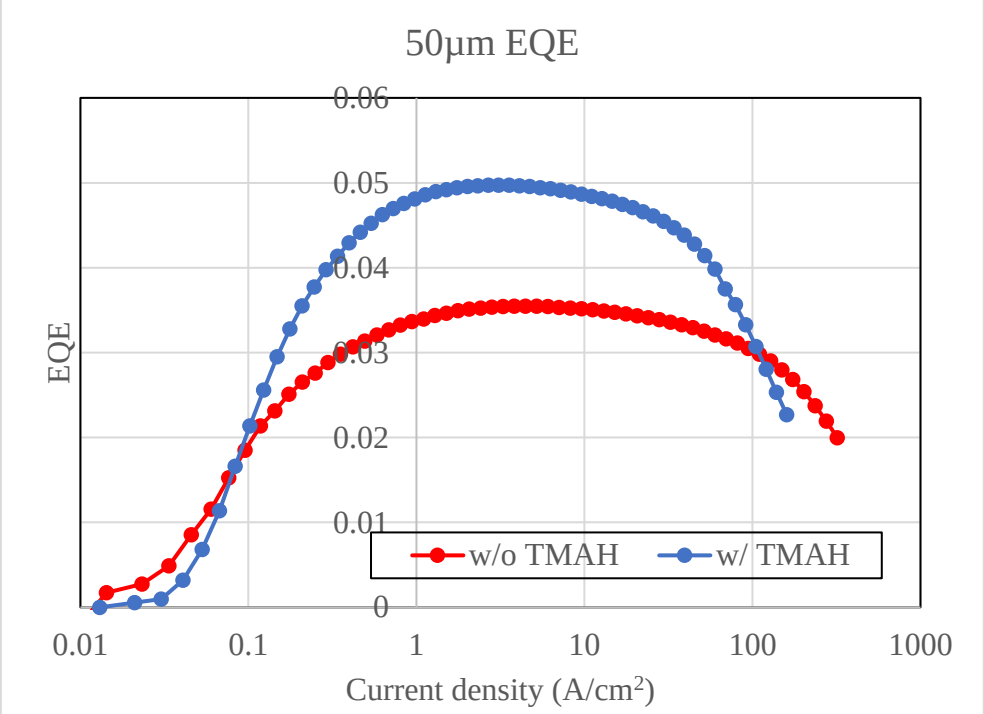

Figure 51 EQE comparison of 50x50μm^2 devices.

doi:10.6342/NTU202500064

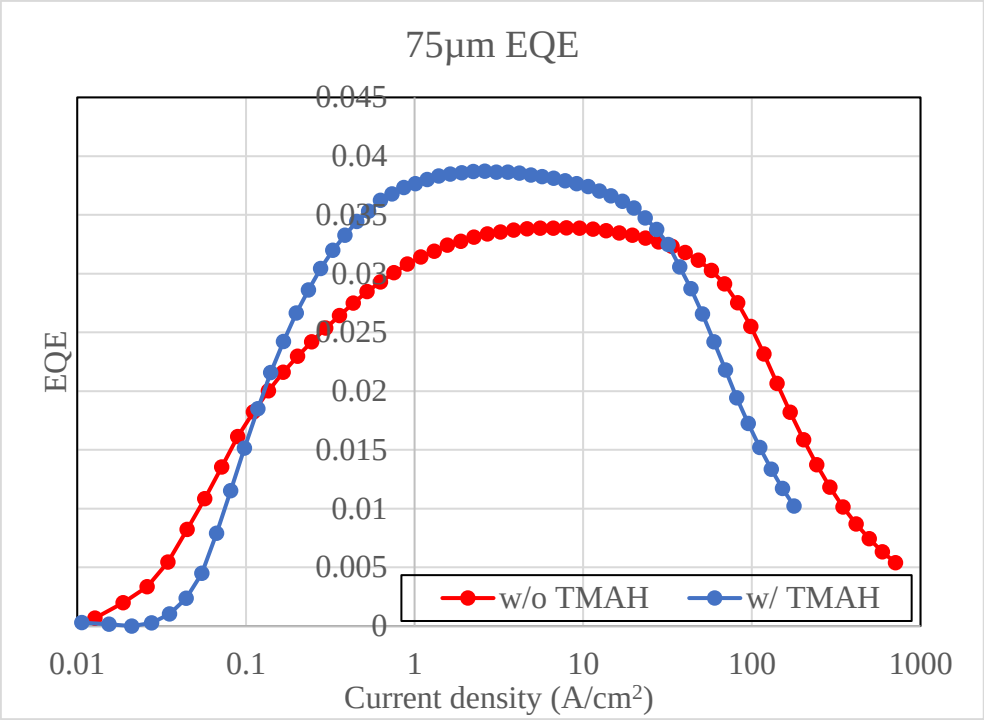

Figure 52 EQE comparison of 75x75μm^2 devices.

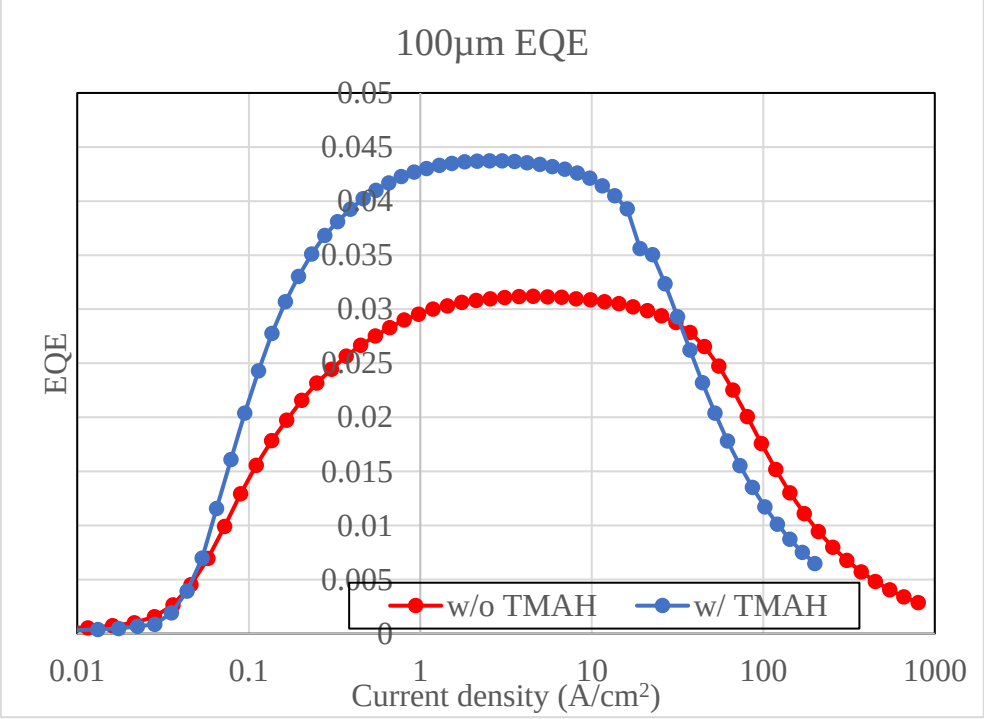

Figure 53 EQE comparison of 100x100μm^2 devices.

doi:10.6342/NTU202500064

Figure 54compares the maximum EQE of all micro-LEDs on the same chart, including the devices we fabricated and those from D. Anis et al. As mentioned earlier, the trend shows that as the mesa size increases, the maximum EQE also increases. The difference is that during our measurements, we may not be able to capture all the photons from larger devices. Therefore, for the larger devices, the maximum EQE of our micro-LEDs does not continue to increase.

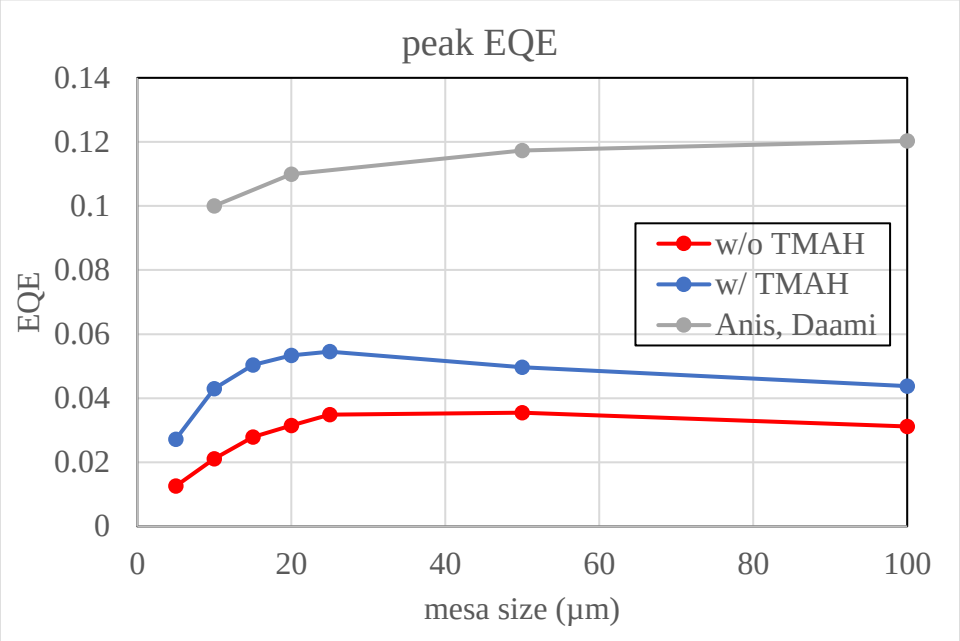

Figure 54 peak EQE comparison of all devices.[32]

doi:10.6342/NTU202500064

4.2.1 Current density at peak EQE (J_{peak})

To differentiate **Equation 3** with respect to the carrier density n, we can obtain the following equation.

$$\frac{d\ EQE}{dn} = LEE \times \frac{B(A - Cn^2)}{(Cn^2 + Bn + A)^2} \qquad \textbf{Equation 4}$$

To find the maximum of EQE, we need to set $\frac{d\ EQE}{dn} = 0$. At this point, n will be $\sqrt{\frac{A}{C}}$.

Also, based on $J = qt(An + Bn^2 + Cn^3)$, we can deduce the relationship between current density J and carrier density n. Therefore, as A becomes smaller, the current density at which the maximum EQE occurs shifts to a lower value. This suggests that when the SRH non-radiative recombination coefficient A is reduced, the device can reach its peak EQE at a lower level of carrier injection or current density.

Since the TMAH treatment reduces the coefficient A, we can observe that the current density corresponding to the maximum EQE for TMAH-treated devices is smaller than that of untreated devices. We can also deduce from this equation that, because the coefficient A is smaller for larger devices, they can achieve the maximum EQE at a lower current density. In **Figure 55**, we similarly compare the peak current density of our

doi:10.6342/NTU202500064

devices with those from D. Anis et al. The same trend can be observed: as the mesa size increases, the peak current density (Jpeak) decreases.

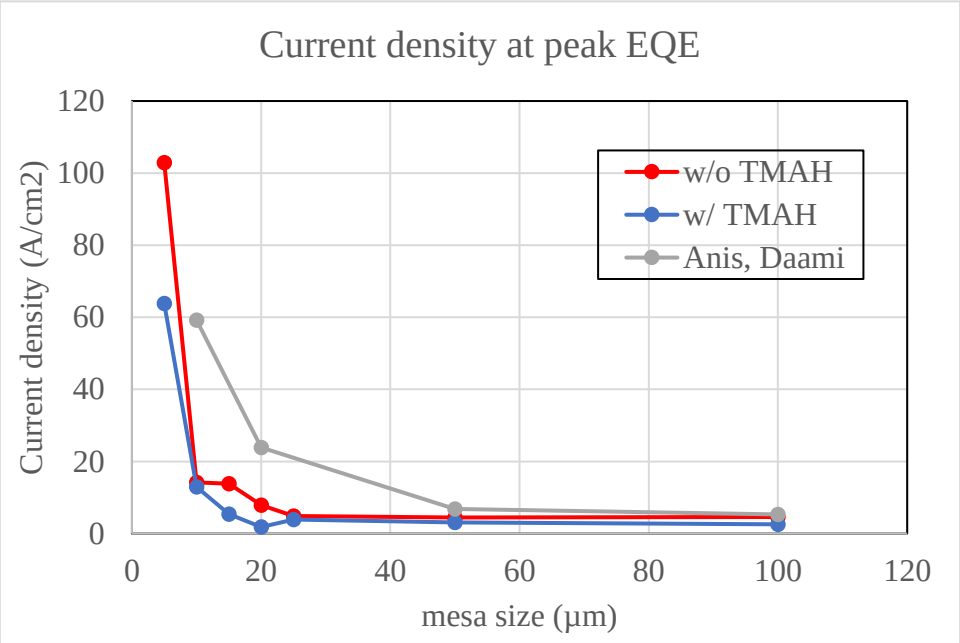

Figure 55 Current density at peak EQE of all devices.[32]

4.3 Spectrum

Due to the small noise in the measurement equipment, the data can affect our determination of the peak wavelength. Therefore, we first apply Gaussian fitting to the measured spectral data before analyzing the results. Below, **Figure 56** and **Figure 57** show the spectra of the 3μm device before and after the fitting, respectively.

doi:10.6342/NTU202500064

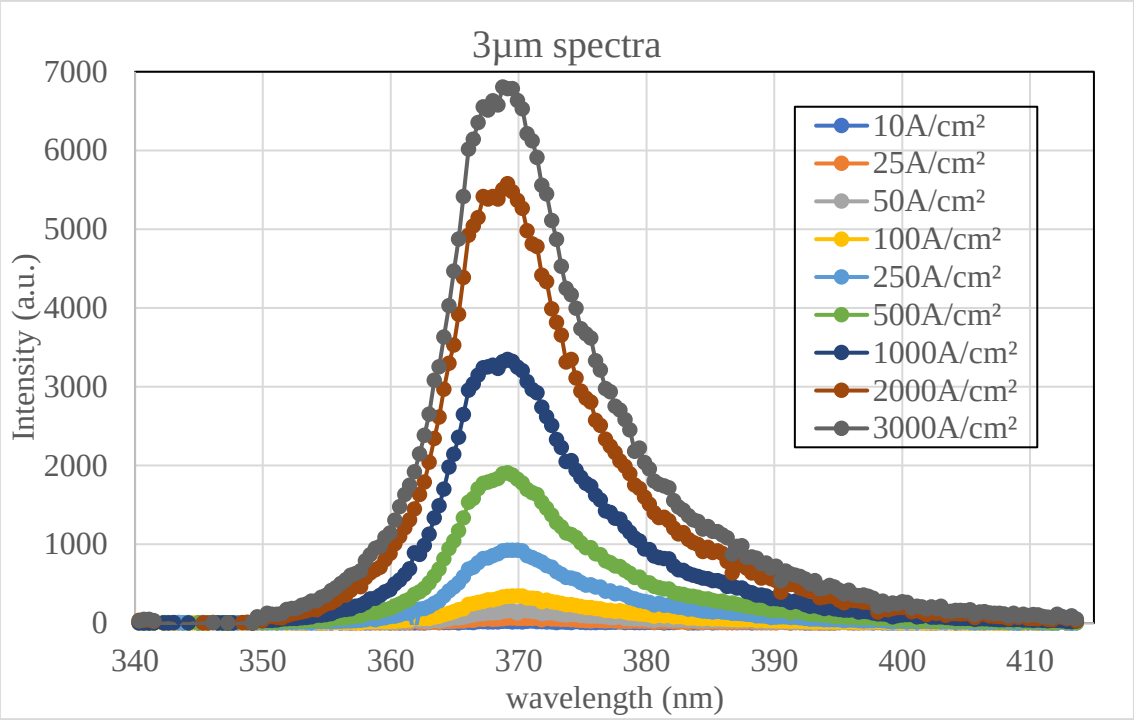

Figure 56 The measured 3μm spectrum.

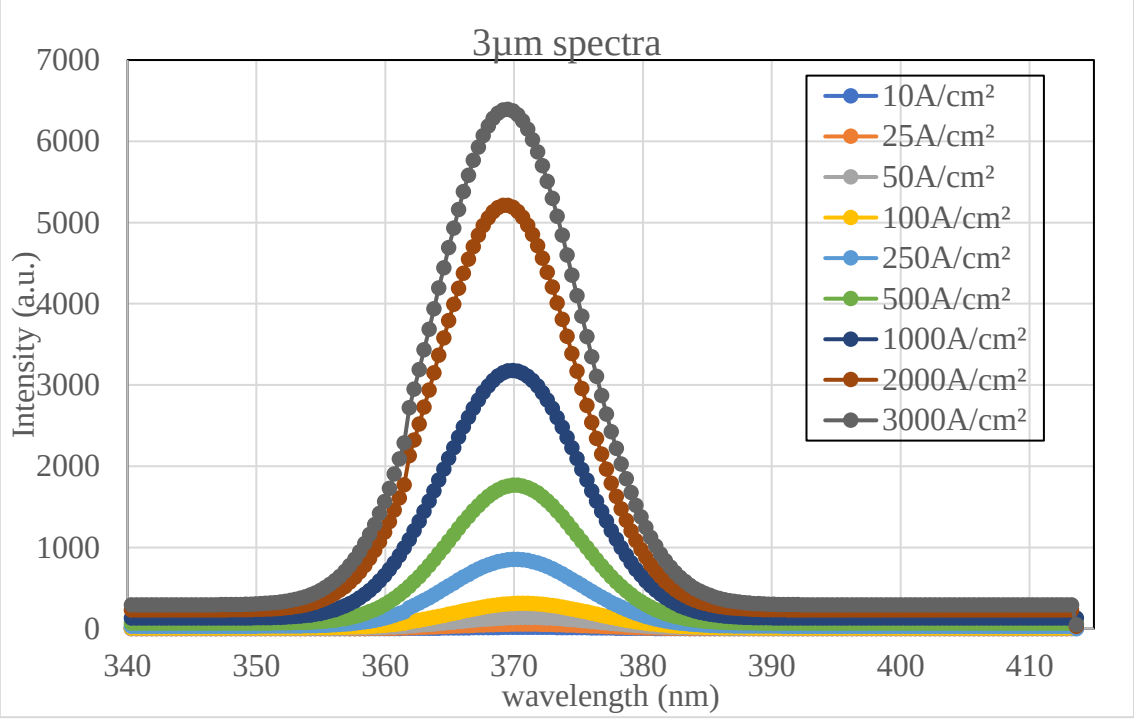

Figure 57 3μm spectrum after Gaussian fitting.

doi:10.6342/NTU202500064

From the experimental data, we observe that the peak wavelength of the emitted light from the LED changes with different current densities. When the wavelength decreases as the current density increases, it is referred to as a blue shift, while the opposite trend is called a red shift.

Within the LED, the Quantum Confined Stark Effect (QCSE) causes the band diagram to distort, bringing the conduction band and valence band closer together. As we begin injecting current and generate a reverse electric field, the screening of the QCSE gradually returns the band diagram to its original state. This causes the energy of the emitted photons to increase, resulting in a blue shift. Additionally, when the number of electrons and holes within the quantum well accumulates to a high level, they recombine from higher energy states, further increasing the photon energy, which also contributes to the blue shift.[33] Next, the self-heating effect refers to the phenomenon where, when a device is injected with high current, the increase in temperature leads to a bandgap shrinkage, which results in a decrease in the energy of the emitted photons, causing a red shift.[34]

From the spectra of the devices below, we can observe that the wavelength of the smaller devices tends to decrease as the current density increases, exhibiting a blue shift. On the

doi:10.6342/NTU202500064

other hand, for the larger devices, as the current density increases, a red shift phenomenon is observed.

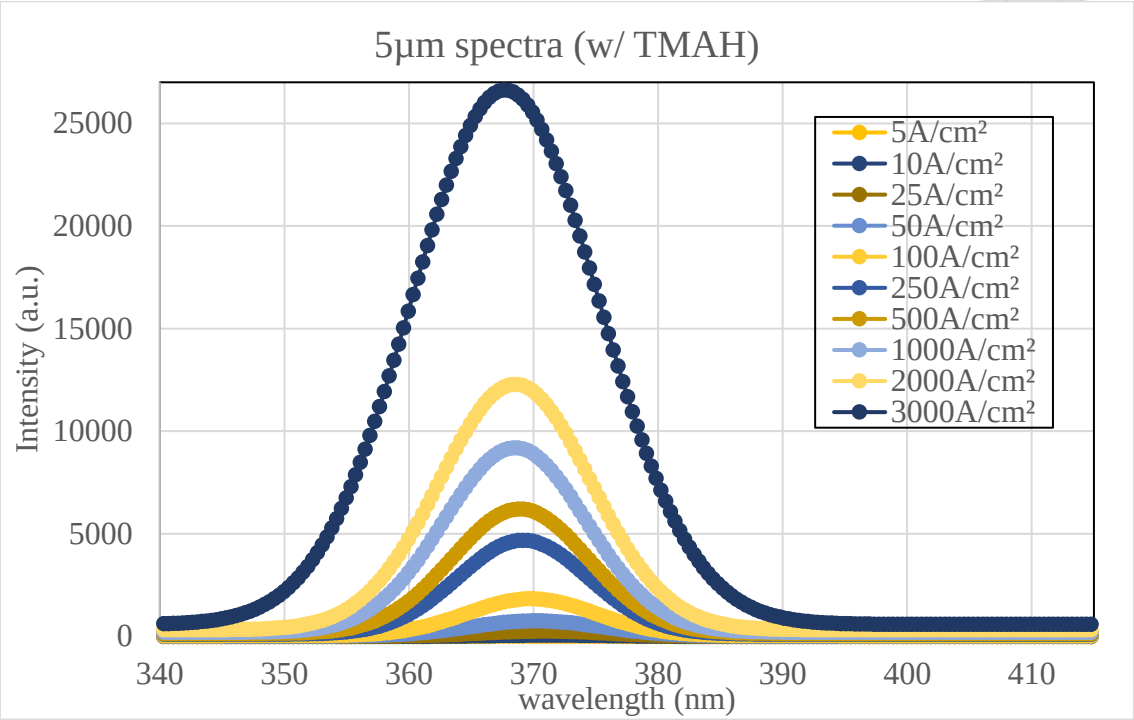

Figure 58 5μm spectra (w/ TMAH).

doi:10.6342/NTU202500064

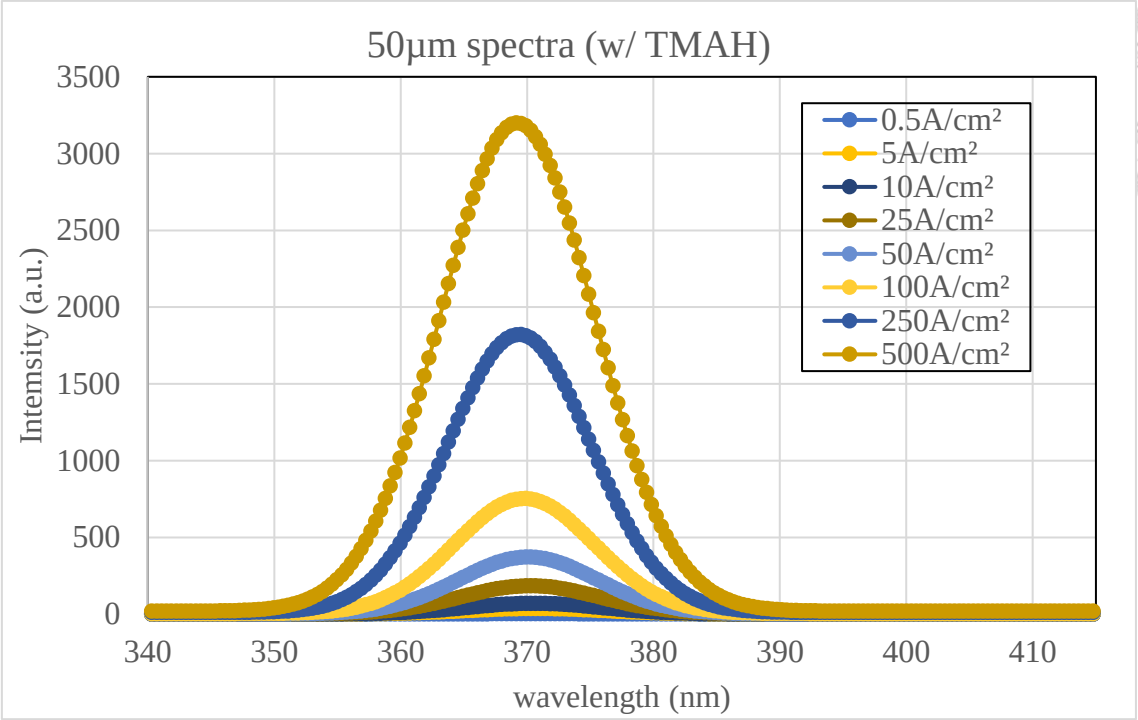

Figure 59 50μm spectra (w/ TMAH).

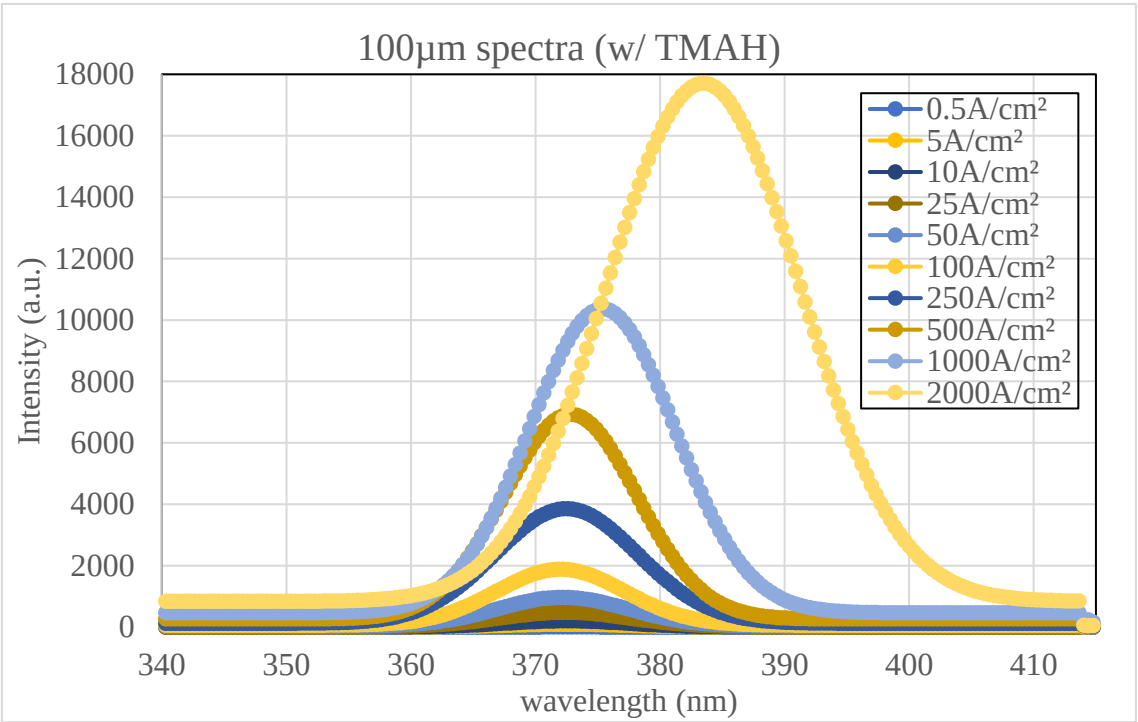

Figure 60 100μm spectra (w/ TMAH).

doi:10.6342/NTU202500064

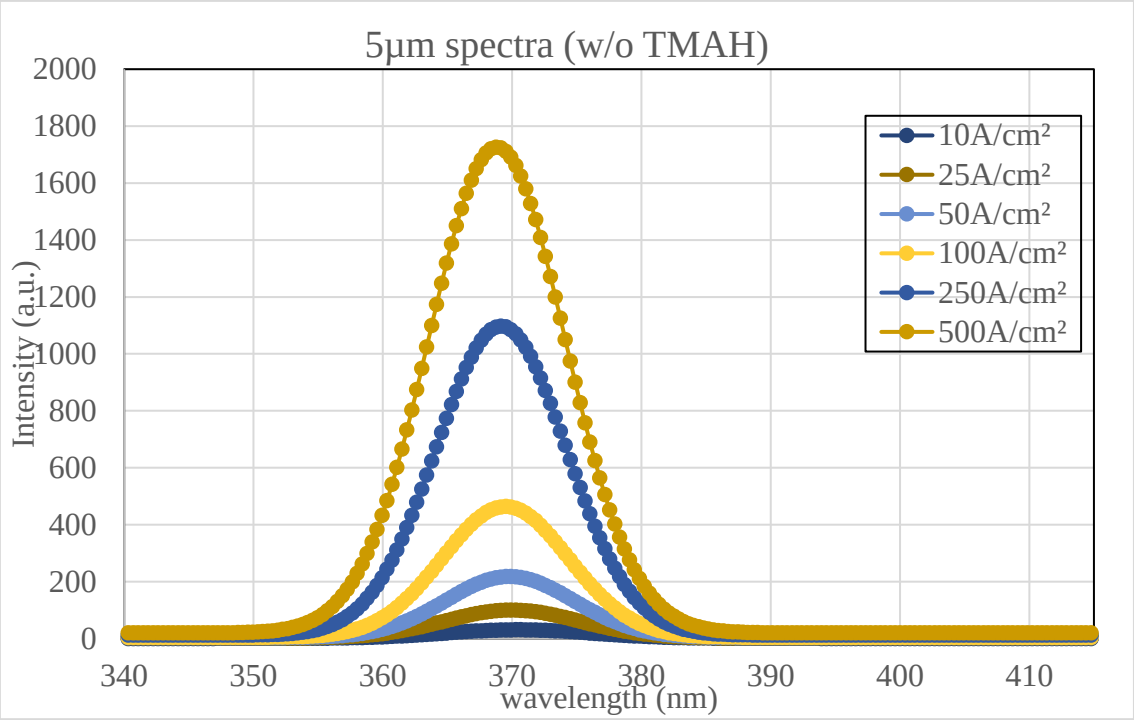

Figure 61 5μm spectra (w/0 TMAH).

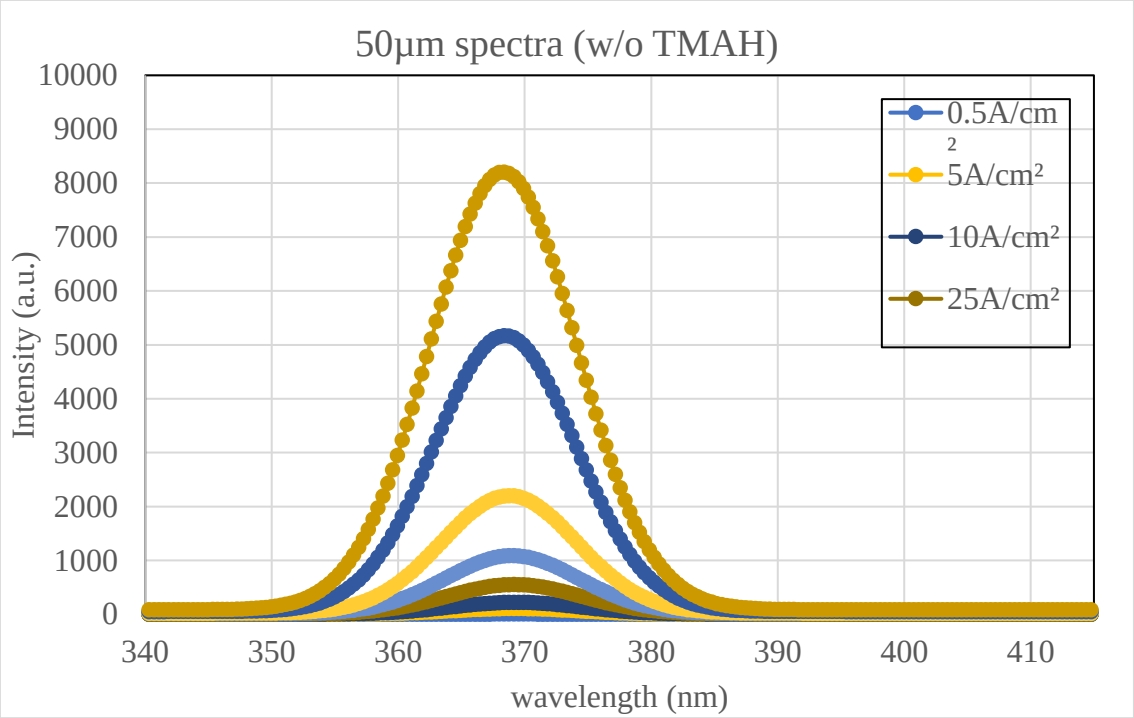

Figure 62 5μm spectra (w/0 TMAH).

doi:10.6342/NTU202500064

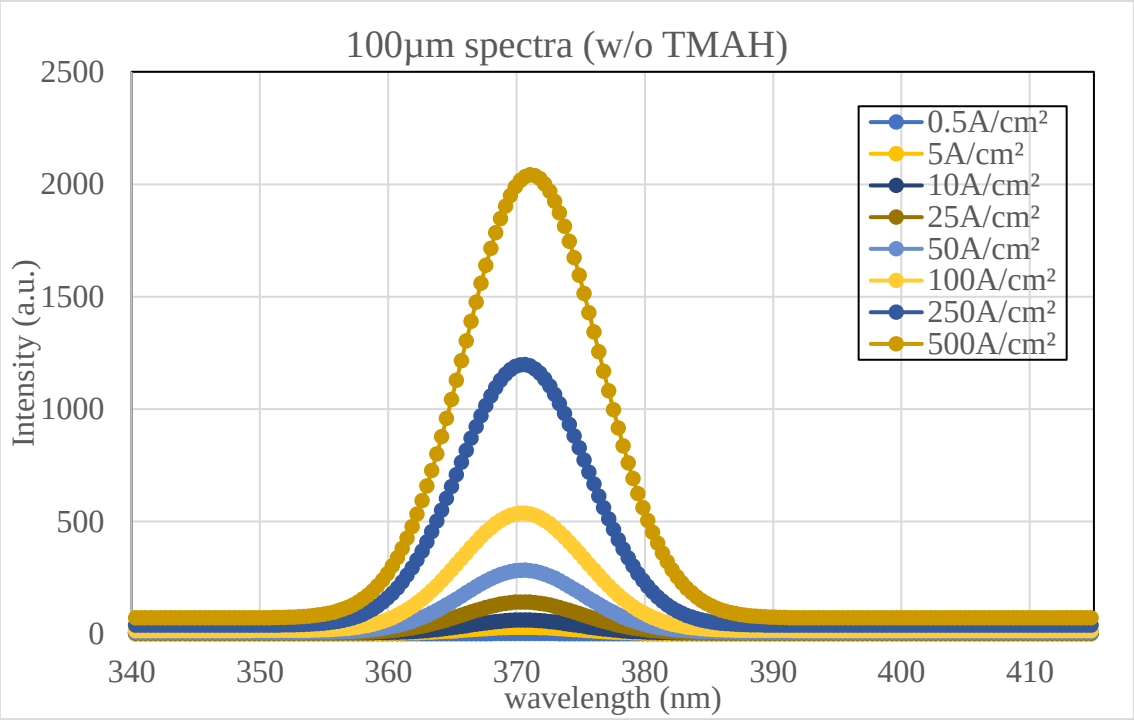

Figure 63 5μm spectra (w/0 TMAH).

4.3.1 Wavelength shift

Figure 64 shows the results from Z. Gong et al.[33], where it is demonstrated that smaller devices exhibit a larger blue shift, and a slight red shift occurs only at higher current densities. For larger devices, the red shift appears at lower current densities. When we look at **Figure 65** and **Figure 66**, which show the wavelength shift of our micro-LEDs, similar results are observed. However, since we were unable to measure such high current densities as they did, the red shift phenomenon has not yet appeared in the smaller devices.

doi:10.6342/NTU202500064

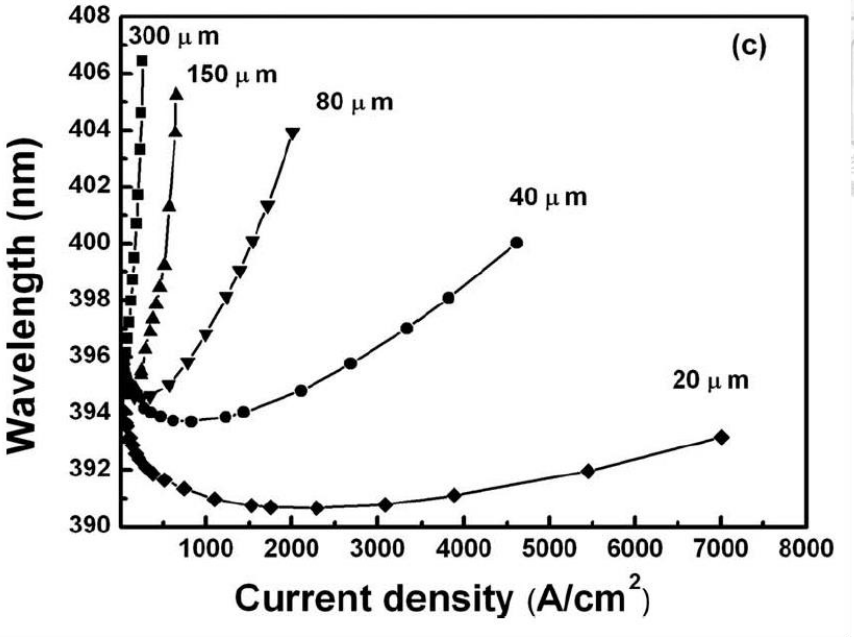

Figure 64 EL shift of changing current density for different mesa sizes.[33]

Generally speaking, larger devices have a smaller ratio of the sidewall surface area to the active volume, which results in poorer sidewall heat dissipation efficiency.[35] As a result, they are more susceptible to the self-heating effect, leading to a red shift.

However, in these two figures, the smallest 3μm and 5μm devices do not follow this trend. A possible reason is that at low current densities, the blue shift is more noticeable. However, at low current densities, the emitted light from the smaller devices is not strong enough, so we are unable to measure the spectrum of the smaller devices at these low current densities. This results in the absence of data from the region where the blue shift

doi:10.6342/NTU202500064

is most prominent in the calculations. Another possible reason is that current density may not fully represent the heat generated by the device. The smallest devices are likely to experience higher power densities at the same current density as other devices due to processing defects, which could result in unexpected heat generation. This may lead to a more severe self-heating effect.

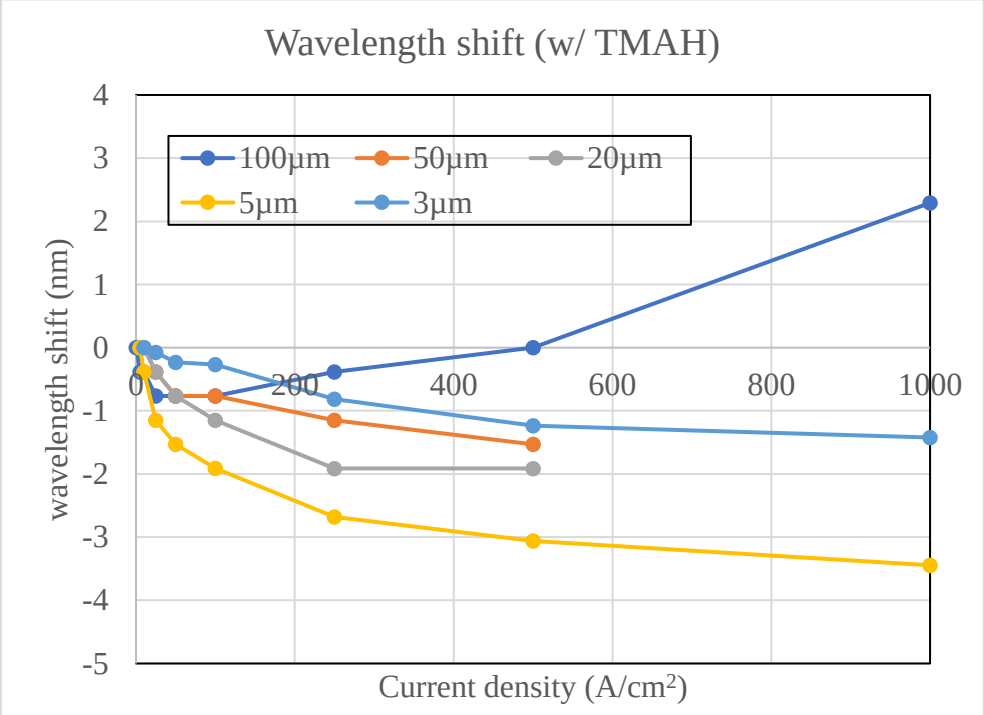

Figure 65 The peak wavelength shift in devices with TMAH treatment.

doi:10.6342/NTU202500064

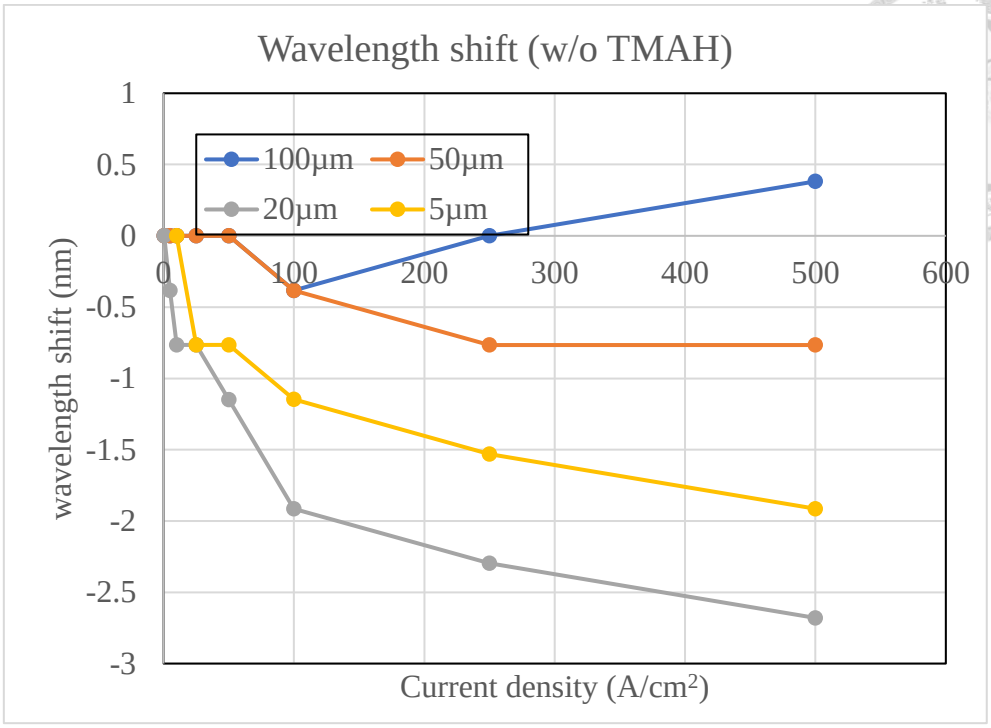

Figure 66 The peak wavelength shift in devices without TMAH treatment.

Next, we will compare the effect of TMAH treatment on the wavelength shift. The following three images show that in devices of the same size, those without TMAH treatment exhibit a smaller blue shift, while the treated ones show a larger blue shift. A possible reason for this phenomenon is that the untreated devices have a higher leakage current, leading to a relatively higher device temperature, which results in a more significant red shift and a smaller blue shift compared to the treated ones.

doi:10.6342/NTU202500064

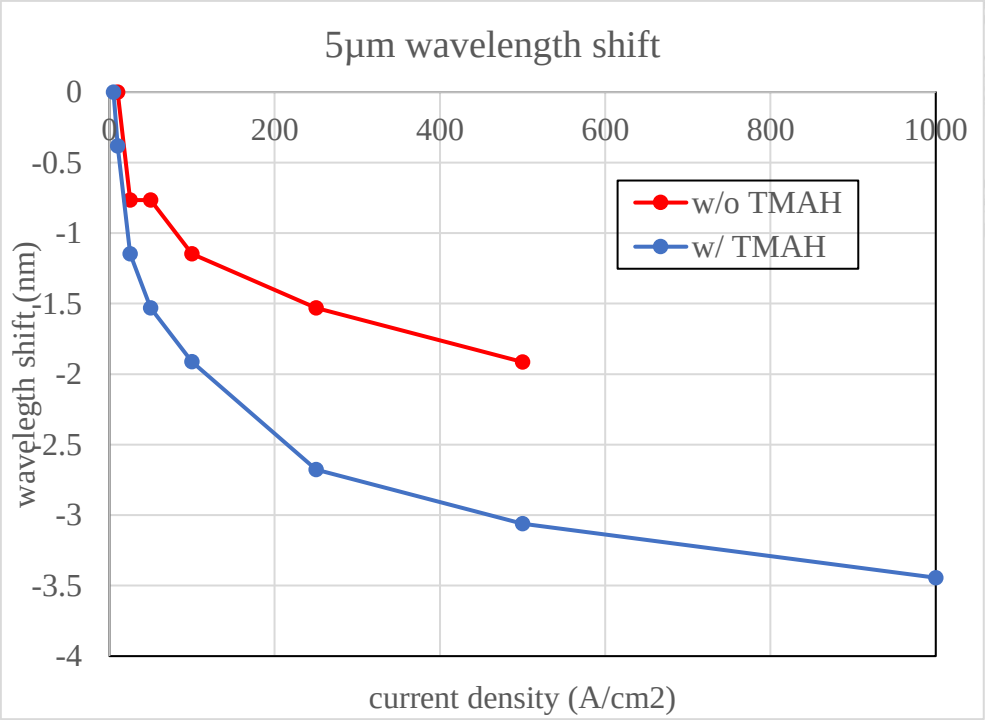

Figure 67 Wavelength shift of the 5μm devices.

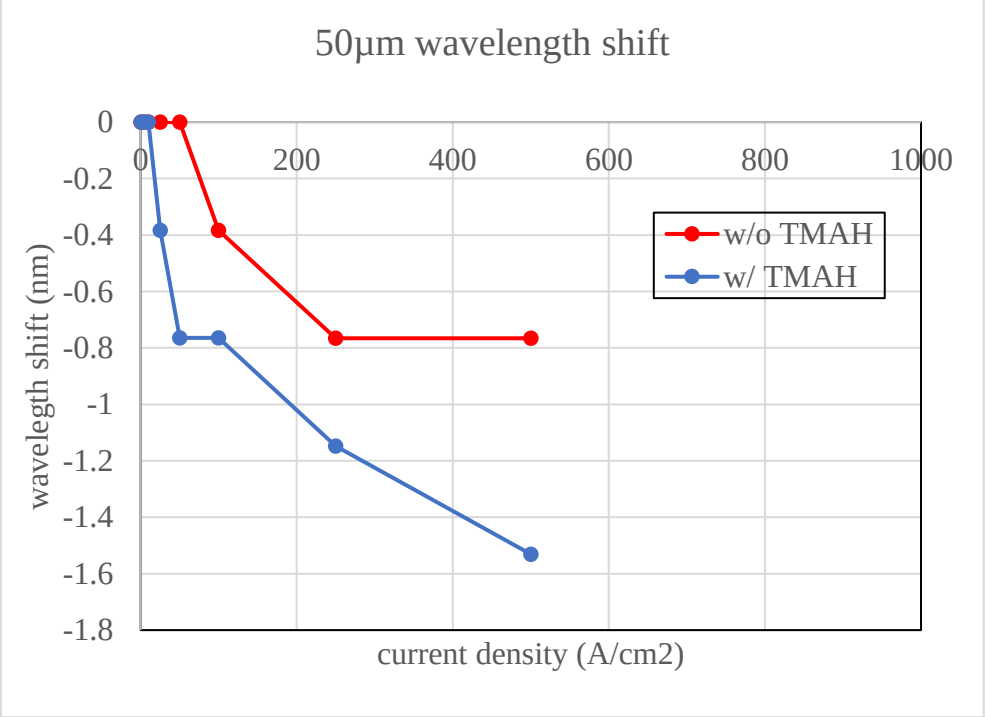

Figure 68 Wavelength shift of the 50μm devices.

doi:10.6342/NTU202500064

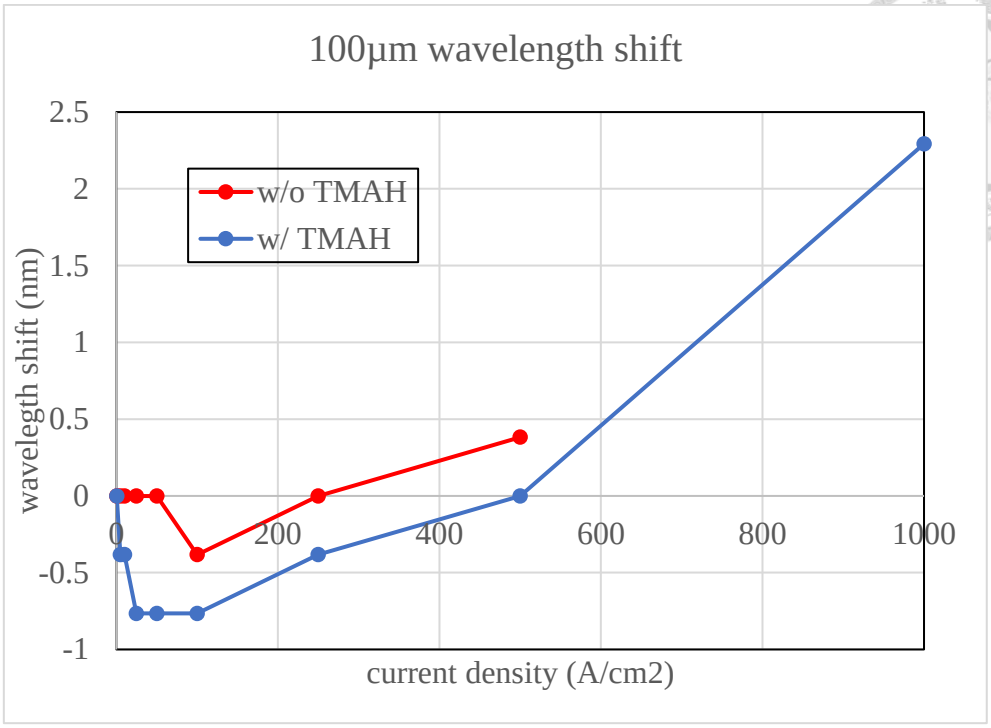

Figure 69 Wavelength shift of the 100μm devices.

doi:10.6342/NTU202500064

Chapter 5 Conclusion and Future Work

5.1 Conclusion

We have fabricated ultraviolet micro-LEDs of various sizes, and through TMAH sidewall treatment, we successfully reduced the device size to 3μm x 3μm. In contrast, the 3μm devices without TMAH treatment were unable to function properly. This sidewall treatment method has made it easier for us to produce smaller devices.

This approach has also improved the electrical properties of our devices. Not only are the IV characteristics more stable, but the leakage current has been reduced, and the ideality factor of the devices is closer to that of an ideal diode.

In terms of EQE performance, the devices after TMAH treatment showed enhanced light emission efficiency and were able to reach their EQE peak at a lower current density.

Furthermore, we also measured their spectra and found that the blue and red shifts are significantly related to the device size. Larger devices, which suffer from severe self-heating, show a red shift as current density increases, while smaller devices exhibit more

doi:10.6342/NTU202500064

stable spectra. Additionally, devices without TMAH treatment experience less blue shift compared to the treated ones due to their relatively larger leakage current.

5.2 Future work

In this experiment, we only discussed the impact of TMAH sidewall treatment on the devices. However, in the future, we may test different TMAH wet etching times and temperatures to determine the optimal parameters for enhancing device performance.

Additionally, due to the size limitation of the photodetector, we were unable to capture all the light emitted by the larger devices. Therefore, in the future, we may need to adjust the position of the photodetector to capture all the photons and avoid measurement distortion. Furthermore, we may also consider increasing the size of the ITO layer, which would allow us to move the P metal pattern away from directly above the mesa, thus reducing the amount of light blocked by the P metal.

Finally, in future spectral measurements, we will need to record the electrical power during testing to more comprehensively discuss the impact of heat on the wavelength shift of the devices

doi:10.6342/NTU202500064

Reference

[1] N. Zheludev, "The life and times of the LED — a 100-year history," *Nature Photonics,* vol. 1, no. 4, pp. 189-192, 2007/04/01 2007, doi: 10.1038/nphoton.2007.34.

[2] E. F. Schubert, *Light-emitting diodes (2018)*. E. Fred Schubert, 2018.

[3] T. Taguchi, "Present Status of Energy Saving Technologies and Future Prospect in White LED Lighting," *IEEJ Transactions on Electrical and Electronic Engineering,* vol. 3, no. 1, pp. 21-26, 2008, doi: https://doi.org/10.1002/tee.20228.

[4] H. X. Jiang and J. Y. Lin, "Nitride micro-LEDs and beyond - a decade progress review," *Opt. Express,* vol. 21, no. S3, pp. A475-A484, 2013/05/06 2013, doi: 10.1364/OE.21.00A475.

[5] J. Day, J. Li, D. Y. C. Lie, C. Bradford, J. Y. Lin, and H. X. Jiang, "III-Nitride full-scale high-resolution microdisplays," *Applied Physics Letters,* vol. 99, no. 3, 2011, doi: 10.1063/1.3615679.

[6] H. Inagaki, A. Saito, H. Sugiyama, T. Okabayashi, and S. Fujimoto, "Rapid inactivation of SARS-CoV-2 with deep-UV LED irradiation," (in eng), *Emerg Microbes Infect,* vol. 9, no. 1, pp. 1744-1747, Dec 2020, doi: 10.1080/22221751.2020.1796529.

[7] P. Tian *et al.*, "AlGaN Ultraviolet Micro-LEDs," *IEEE Journal of Quantum Electronics,* vol. 58, no. 4, pp. 1-14, 2022, doi: 10.1109/JQE.2022.3159854.

[8] H.-V. Han *et al.*, "Resonant-enhanced full-color emission of quantum-dot-based micro LED display technology," *Opt. Express,* vol. 23, no. 25, pp. 32504-32515, 2015/12/14 2015, doi: 10.1364/OE.23.032504.

doi:10.6342/NTU202500064

[9] Y. Li *et al.*, "Effective suppression of interface states in recessed-gate MIS-HEMTs by TMAH wet etching," *Applied Physics Express,* vol. 17, no. 1, p. 011004, 2023/12/29 2024, doi: 10.35848/1882-0786/ad1199.

[10] Y. J. Yoon *et al.*, "TMAH-based wet surface pre-treatment for reduction of leakage current in AlGaN/GaN MIS-HEMTs," *Solid-State Electronics,* vol. 124, pp. 54-57, 2016/10/01/ 2016, doi: https://doi.org/10.1016/j.sse.2016.06.009.

[11] M. Cinquino *et al.*, "Light-Emitting Textiles: Device Architectures, Working Principles, and Applications," *Micromachines*, vol. 12, no. 6, doi: 10.3390/mi12060652.

[12] "Light Emitting Diode (LED)." https://byjus.com/physics/light-emitting-diode/ (accessed.

[13] G. Bizjak, K. Malovrh Rebec, M. Kobav, and M. Klanjšek Gunde, *Photobiological aspects of LED sources for general lighting*. 2012.

[14] "diode IV." https://www.allaboutcircuits.com/technical-articles/understanding-i-v-curves-of-non-linear-devices/ (accessed.

[15] D. Hwang, A. Mughal, C. D. Pynn, S. Nakamura, and S. P. DenBaars, "Sustained high external quantum efficiency in ultrasmall blue III–nitride micro-LEDs," *Applied Physics Express,* vol. 10, no. 3, p. 032101, 2017.

[16] M. S. Wong *et al.*, "Improved performance of AlGaInP red micro-light-emitting diodes with sidewall treatments," *Opt. Express,* vol. 28, no. 4, pp. 5787-5793, 2020/02/17 2020, doi: 10.1364/OE.384127.

[17] J. Kou *et al.*, "Impact of the surface recombination on InGaN/GaN-based blue micro-light emitting diodes," *Opt. Express,* vol. 27, no. 12, pp. A643-A653, 2019/06/10 2019, doi: 10.1364/OE.27.00A643.

doi:10.6342/NTU202500064

[18] T.-Y. Lee *et al.*, "Increase in the efficiency of III-nitride micro LEDs by atomic layer deposition," *Opt. Express,* vol. 30, no. 11, pp. 18552-18561, 2022/05/23 2022, doi: 10.1364/OE.455726.

[19] R. T. Tung, "Recent advances in Schottky barrier concepts," *Materials Science and Engineering: R: Reports,* vol. 35, no. 1, pp. 1-138, 2001/11/09/ 2001, doi: https://doi.org/10.1016/S0927-796X(01)00037-7.

[20] D. Neamen, *Semiconductor Physics And Devices*. McGraw-Hill Education, 2003.

[21] X. Guo and E. F. Schubert, "Current crowding and optical saturation effects in GaInN/GaN light-emitting diodes grown on insulating substrates," *Applied Physics Letters,* vol. 78, no. 21, pp. 3337-3339, 2001, doi: 10.1063/1.1372359.

[22] X. Guo and E. Schubert, "Current crowding in GaN/InGaN light emitting diodes on insulating substrates," *Journal of applied Physics,* vol. 90, no. 8, pp. 4191-4195, 2001.

[23] J. M. Quero, F. Perdigones, and C. Aracil, "11 - Microfabrication technologies used for creating smart devices for industrial applications," in *Smart Sensors and MEMs (Second Edition)*, S. Nihtianov and A. Luque Eds.: Woodhead Publishing, 2018, pp. 291-311.

[24] A. Anbari, H. T. Chien, S. Datta, W. Deng, D. Weitz, and J. Fan, "Microfluidic Model Porous Media: Fabrication and Applications," *Small,* vol. 14, p. 1703575, 03/12 2018, doi: 10.1002/smll.201703575.

[25] B. Chen, F. Tay, and C. Iliescu, "Development of thick film PECVD Amorphous silicon with low stress for MEMS applications," *Proceedings of SPIE - The International Society for Optical Engineering,* vol. 7269, 12/01 2008, doi: 10.1117/12.810441.

doi:10.6342/NTU202500064

[26] A. Bashir, T. I. Awan, A. Tehseen, M. B. Tahir, and M. Ijaz, "Chapter 3 - Interfaces and surfaces," in *Chemistry of Nanomaterials*, T. I. Awan, A. Bashir, and A. Tehseen Eds.: Elsevier, 2020, pp. 51-87.

[27] J.-H. Park *et al.*, "Impact of Sidewall Conditions on Internal Quantum Efficiency and Light Extraction Efficiency of Micro-LEDs," *Advanced Optical Materials,* vol. 11, no. 10, p. 2203128, 2023/05/01 2023, doi: https://doi.org/10.1002/adom.202203128.

[28] H. Masui, "Diode ideality factor in modern light-emitting diodes," *Semiconductor Science and Technology,* vol. 26, no. 7, p. 075011, 2011/04/11 2011, doi: 10.1088/0268-1242/26/7/075011.

[29] J. M. Shah, Y.-L. Li, T. Gessmann, and E. F. Schubert, "Experimental analysis and theoretical model for anomalously high ideality factors (n≫2.0) in AlGaN/GaN p-n junction diodes," *Journal of Applied Physics,* vol. 94, no. 4, pp. 2627-2630, 2003, doi: 10.1063/1.1593218.

[30] M. Siva Pratap Reddy, D.-H. Son, J.-H. Lee, J.-S. Jang, and V. Rajagopal Reddy, "Influence of tetramethylammonium hydroxide treatment on the electrical characteristics of Ni/Au/GaN Schottky barrier diode," *Materials Chemistry and Physics,* vol. 143, no. 2, pp. 801-805, 2014/01/15/ 2014, doi: https://doi.org/10.1016/j.matchemphys.2013.10.016.

[31] T. Gotow, T. Arai, T. Aota, and Y. Miyamoto, "Evaluation of TMAH treatment for isolation process of N-polar GaN HEMTs," in *2022 Compound Semiconductor Week (CSW)*, 1-3 June 2022 2022, pp. 1-2, doi: 10.1109/CSW55288.2022.9930366.

[32] D. Anis and O. François, "InGaN/GaN µLED SPICE modelling with size-dependent ABC model integration," in *Proc.SPIE*, 2019, vol. 10912, p. 109120E, doi: 10.1117/12.2509382. [Online]. Available: https://doi.org/10.1117/12.2509382

doi:10.6342/NTU202500064

[33] Z. Gong *et al.*, "Size-dependent light output, spectral shift, and self-heating of 400 nm InGaN light-emitting diodes," *Journal of Applied Physics,* vol. 107, no. 1, 2010, doi: 10.1063/1.3276156.

[34] V. M. Krasnov, A. Yurgens, D. Winkler, and P. Delsing, "Self-heating in small mesa structures," *Journal of Applied Physics,* vol. 89, no. 10, pp. 5578-5580, 2001, doi: 10.1063/1.1367880.

[35] H.-S. Chen *et al.*, "Mesa-size-dependent color contrast in flip-chip blue/green two-color InGaN/GaN multi-quantum-well micro-light-emitting diodes," *Applied Physics Letters,* vol. 89, no. 9, 2006, doi: 10.1063/1.2339034.

doi:10.6342/NTU202500064